

Constraining Dark Matter Annihilation with Cosmic Ray Antiprotons using Neural Networks

Felix Kahlhoefer,¹ Michael Korsmeier,² Michael Krämer,¹ Silvia Manconi¹ and Kathrin Nippel¹

¹Institute for Theoretical Particle Physics and Cosmology (TTK), RWTH Aachen University, D-52056 Aachen, Germany

²The Oskar Klein Centre for Cosmoparticle Physics, Department of Physics, Stockholm University, Alba Nova, 10691 Stockholm, Sweden

E-mail: kahlhoefer@physik.rwth-aachen.de, mkraemer@physik.rwth-aachen.de,
michael.korsmeier@fysik.su.se, manconi@physik.rwth-aachen.de,
nippel@physik.rwth-aachen.de

Abstract. The interpretation of indirect detection experiments searching for dark matter annihilations requires computationally expensive simulations of cosmic-ray propagation. In this work we present a new method based on Recurrent Neural Networks that significantly accelerates simulations of secondary and dark matter cosmic ray antiprotons while achieving excellent accuracy. This approach allows for an efficient profiling or marginalization over the nuisance parameters of a cosmic ray propagation model in order to perform parameter scans for a wide range of dark matter models. We identify importance sampling as particularly suitable for ensuring that the network is only evaluated in well-trained parameter regions. We present resulting constraints using the most recent AMS-02 antiproton data on several models of Weakly Interacting Massive Particles. The fully trained networks are released as DarkRayNet together with this work and achieve a speed-up of the runtime by two orders of magnitude compared to conventional approaches.

Keywords: dark matter simulations, cosmic ray theory

Preprint numbers: TTK-21-XX

Contents

1	Introduction	1
2	Cosmic-ray antiprotons in the Galaxy	3
2.1	Antiprotons from dark matter annihilation	3
2.2	Secondary antiprotons	4
2.3	Propagation in the Galaxy and solar modulation	5
2.4	Fit to AMS-02 data	7
3	Deep Neural Network Setup and Training	10
3.1	Training Set	11
3.2	Neural Network Architectures	11
3.3	Training process	14
3.4	Validation of the Network Performance	16
4	Constraining the Dark Matter Annihilation Cross Section	18
4.1	Statistical method	18
4.2	Example A: Single Dark Matter Annihilation Channel	20
4.3	Example B: Scalar Singlet Dark Matter	23
5	Conclusions	25
A	Predicting Proton and Helium Spectra	26

1 Introduction

The central prediction of the WIMP paradigm is that Dark Matter (DM) particles should have a thermally averaged annihilation cross section of $\langle\sigma v\rangle \sim 10^{-26} \text{ cm}^3 \text{ s}^{-1}$ during freeze-out. In many DM models, the present-day annihilation cross section in astrophysical systems is predicted to be of a similar magnitude, providing a clear target for indirect detection experiments searching for the products of DM annihilation processes.

While the most robust constraints on the DM annihilation cross section stem from observations of the γ -ray sky, in particular from Fermi-LAT [1–3], highly complementary information can be obtained by precisely measuring the flux of charged anti-particles arriving on Earth. Very recently, AMS-02 has released results from the first seven years of data taking [4], which include in particular the flux of antiprotons with unprecedented precision. Theoretical predictions for this flux however require detailed modelling of the production and propagation of charged cosmic rays (CRs) in the Galaxy, which are subject to significant uncertainties.

While various numerical codes, such as GALPROP [5] and DRAGON [6], exist to address this challenge and simulate the propagation of CRs, they require as input a large number of parameters that need to be varied to assess their impact on the predictions. As a result these simulations are typically computationally so expensive that they become prohibitive in the context of a global analysis of DM models, where also the fundamental model parameters

need to be varied. Recent analyses of the AMS-02 antiproton data have therefore typically focused on simplified DM models with only a single annihilation channel, see e.g. [7–10].

In the present work we explore the potential of artificial neural networks (ANNs) to solve this issue and substantially speed up the calculation of predictions for the primary antiproton flux for a very broad range of DM models. Specifically, we employ recurrent neural networks (RNNs), which are particularly well suited for the prediction of continuous spectra. The network is trained on a large sample of antiproton fluxes based on propagation parameters that are chosen to broadly agree with recent AMS-02 data, and a general parametrisation of the properties of the DM particle in terms of its mass and the branching fractions for various different final states. Using the same approach we have also developed and trained ANNs to accurately predict further CR species, like secondary antiprotons, protons or helium.

The predictions of the network can then be used to calculate the likelihood of the AMS-02 data for a given DM model and varying propagation parameters in order to calculate exclusion limits using a range of frequentist or Bayesian methods. However, it is important to ensure that the resulting constraints are not biased by regions of parameter space for which the ANN has not been sufficiently trained. In the present work this potential pitfall is avoided by evaluating the likelihood for a fixed sample of propagation parameter points drawn from the posterior probability distribution in the absence of a DM signal. The marginalisation over propagation uncertainties can then be performed via importance sampling, i.e. by appropriately reweighing and combining the points in the sample. This approach is particularly well suited for the analysis of antiproton data, since the propagation parameters are rather tightly constrained by the proton flux and the secondary antiproton flux, so that the presence of a DM signal does not dramatically shift the relevant regions of parameter space.

We emphasise that, while the initial generation of a sample from the posterior is computationally expensive, it does not require specific assumptions on the properties of DM and therefore only needs to be carried out once in advance. Moreover, the same simulation step can be used to set up the training data for the ANN, ensuring that the network is trained specifically on the most interesting regions of parameter space. Once training is completed, the remaining steps are computationally cheap and can be performed for a large number of DM parameters. Indeed, the full marginalisation over propagation parameters can be performed in a similar amount of time as it would take to simulate a single parameter point in the conventional approach.

We apply our fully trained ANN to a number of cases of particular interest. For the case of DM annihilations exclusively into bottom quarks we show that the most recent AMS-02 data leads to results that are compatible with previous studies. In particular, we recover a notable excess for DM masses around 100 GeV in the case that no correlations in the AMS-02 data are considered. We also present new constraints on the well-studied model of scalar singlet DM and find that antiproton data places competitive constraints on this model. However, we emphasise that the ANN is not limited to these cases and can be applied to a wide variety of DM models. Moreover, the general approach that we present can be extended to consider different propagation models (provided a suitable simulator exists), systematic uncertainties (such as correlations in the AMS-02 data) or cross-section uncertainties, enabling the community to fully explore the wealth of the available CR data.

The remainder of this work is structured as follows. In section 2 we briefly review the fundamental concepts of CR production and propagation and present the specific implementation that we adopt in the present work. We also carry out a first analysis of the most recent AMS-02 data and perform a parameter scan to identify the most interesting regions of parameter

space. In section 3 we introduce our machine learning approach to simulating CRs and discuss how we train and validate our ANNs. Finally, in section 4 we apply the fully trained ANNs to constrain DM models. We present the relevant statistical methods and discuss the resulting exclusion limits.

2 Cosmic-ray antiprotons in the Galaxy

For the following discussion it is useful to distinguish between primary and secondary CRs. Primary CRs are directly accelerated and emitted by standard astrophysical sources like supernova remnants or pulsars. But also more exotic scenarios such as the production of (anti)particles by DM annihilation or decay are considered as primary origin. Protons provide the dominant contribution to primary CRs (about 90%) while helium (He) makes up about 10%. Heavier nuclei only contribute at the percent level. On the other hand, secondary CRs are produced during the propagation of primary CRs by fragmentation or decay. More specifically, when the primary CRs interact with the gas in the Galactic disc, commonly called interstellar medium (ISM), secondary particles are produced. Because of the different production mechanism, secondaries are suppressed with respect to primary CRs. It is commonly believed that CR antiprotons do not have standard astrophysical sources¹ such that their dominant contribution comes from secondary production. As a consequence, antiprotons are suppressed by 4–5 orders of magnitude with respect to protons, which makes them (together with other antimatter CRs, e.g. antideuterons [14, 15]) a promising channel for constraining DM signals.

In this section we first discuss the production of antiprotons in the annihilation of dark matter particles in our Galaxy, followed by a discussion of backgrounds from secondary antiprotons. We then present the framework that we use to simulate CR propagation and the strategy to fit the resulting spectra to data. Finally, we perform a scan over the propagation parameters in order to create the training set for the machine learning approach introduced in section 3.

2.1 Antiprotons from dark matter annihilation

CR antiprotons are a long standing target used to search for signals of WIMP DM in our Galaxy [16–31]. More recently, there has been a discussion of an antiproton excess at about 20 GeV, which could be fitted with a primary DM source [7–10, 32]. However, the excess might also be accounted for by a combination of systematic effects [33–35]. If DM particles annihilate into standard model particle final states f within the diffusion halo of our Galaxy as $\text{DM} + \text{DM} \rightarrow f + \bar{f}$, we expect a corresponding flux contribution to antiprotons in CRs, coming from the subsequent decay of for example $q + \bar{q}$ modes (see e.g. [36]). The source term of this primary antiproton component, $q_{\bar{p}}^{(\text{DM})}$, is a function of the Galactic coordinates \mathbf{x} and the antiproton kinetic energy E_{kin} . For a generic combination of standard model final states f it reads:

$$q_{\bar{p}}^{(\text{DM})}(\mathbf{x}, E_{\text{kin}}) = \frac{1}{2} \left(\frac{\rho(\mathbf{x})}{m_{\text{DM}}} \right)^2 \sum_f \langle \sigma v \rangle_f \frac{dN_{\bar{p}}^f}{dE_{\text{kin}}} . \quad (2.1)$$

¹We note that the possibility of primary antiprotons that are directly produced and accelerated at SNRs [11–13] is also discussed in literature.

The factor $1/2$ in eq. (2.1) corresponds to Majorana fermion DM. Furthermore, m_{DM} is the DM mass, $\rho(\mathbf{x})$ the DM halo energy density profile, and $\langle \sigma v \rangle_f$ is the thermally averaged annihilation cross section. Finally, $dN_{\bar{p}}^f/dE_{\text{kin}}$ denotes the energy spectrum of antiprotons for a single DM annihilation. This quantity depends on the DM mass and the standard model final state. Here we implement the widely used tabulated results for the antiproton energy spectrum presented in Ref. [36] which include electroweak corrections.²

We assume that the DM density in our Galaxy follows an NFW profile [38] $\rho_{\text{NFW}}(r) = \rho_h r_h / r (1 + r/r_h)^{-2}$, with a scale radius of $r_h = 20$ kpc and a characteristic halo density, ρ_h , which is normalized such that the local DM density at the solar position of 8.5 kpc is fixed to 0.43 GeV/cm^3 [39], compatible also with more recent estimates [40]. We note that the NFW profile is only one of many viable DM profiles currently investigated. Other profiles can have a significantly different behavior towards the Galactic center, see e.g. the discussion in Ref. [41]. However, we stress that choosing a different DM density profile only has a small impact on the results presented in this paper since CR antiprotons from DM annihilation dominantly arrive from the local environment. Therefore they are mostly sensitive to the local DM density and the resulting flux depends only weakly on the shape of the DM density profile at the Galactic center. More specifically, the impact of changing the cuspy NFW profile to the cored Burkert profile [42] has been quantified in Ref. [43]; it was found that a core radius of 5 kpc only weakens DM limits by about 20%.

2.2 Secondary antiprotons

The ISM consists of roughly 90% hydrogen (H) and 10% He. Thus secondary antiprotons are mostly produced by the interaction of p and He CRs with the H and He components of the ISM. The source term for the secondary antiprotons $q_{\bar{p}}^{(\text{sec})}$ is thus given by the convolution of the primary CR fluxes ϕ of isotope i , the ISM density n_{ISM} of component $j \in \{\text{H, He}\}$, and the energy-differential production cross section $d\sigma_{ij \rightarrow \bar{p}}/dE_{\text{kin},\bar{p}}$:

$$q_{\bar{p}}^{(\text{sec})}(\mathbf{x}, E_{\text{kin},\bar{p}}) = \sum_{j \in \{\text{H, He}\}} 4\pi n_{\text{ISM},j}(\mathbf{x}) \sum_i \int dE_{\text{kin},i} \phi_i(E_{\text{kin},i}) \frac{d\sigma_{ij \rightarrow \bar{p}}}{dE_{\text{kin},\bar{p}}}(E_{\text{kin},i}, E_{\text{kin},\bar{p}}). \quad (2.2)$$

By construction, secondaries are suppressed with respect to primary CRs. In the case of antiprotons, the experimentally observed suppression compared to protons is 4–5 orders of magnitude. Since secondary CRs constitute the dominant contribution of the measured antiproton flux, considering standard astrophysical sources only already results in a good fit to the data, see also discussion in Sec. 2.4.

The cross section of secondary antiproton production is a very important ingredient of eq. (2.2), which has been discussed by various groups recently [44–47]. In general there are two different strategies to determine this cross section. On the one hand, Monte Carlo generators, which are tuned to the relevant cross section data [47], can be used to infer the relevant cross section. On the other hand, a parametrization of the Lorentz invariant cross section can be fitted to all available cross section data. Then the required energy-differential cross section is obtained by an angular integration [44–46]. We follow the second approach and use the analytic cross section parametrization from Ref. [45] with the updated parameters from Ref. [46]. An important advantage of the analytic cross section parametrization is that

²If DM annihilates into a pair of W or Z bosons it is possible to produce one of them off-shell. This possibility is not taken into account in the original tables. We extend the tables of W and Z bosons to lower DM masses using the tables from Ref. [37].

it is explicitly tuned to cross-section data at low energies, and therefore more reliable below antiproton energies of ~ 10 GeV as discussed in Ref. [48].

Finally, we consider that secondary antiprotons may scatter inelastically with the ISM and lose energy. This antiproton contribution, commonly referred to as tertiary [49], is suppressed with respect to the secondaries.

2.3 Propagation in the Galaxy and solar modulation

The sources, acceleration and propagation of Galactic CRs are research topics by themselves [50, 51]. Fast evolution and progresses has been driven in the last years by newly available and very precise data by AMS-02 [4], PAMELA [52] and Voyager [53]. Some recent developments include the studies of systematic uncertainties from solar modulation, correlated experimental data points, secondary production/fragmentation cross sections as well as detailed studies of propagation phenomena below a rigidity of 10 GV to disentangle diffusion and reacceleration [54–64]. Here we will not explore these exciting directions and instead focus on one standard setup of CR propagation, which was already studied in the context DM searches with antiprotons in Ref. [32]. The machine learning approach and the statistical methods introduced below can however be readily applied also to alternative assumptions and more refined descriptions. We briefly summarize below the main ingredients of this specific approach and refer to [32] for a more detailed discussion.

Charged CRs propagate within a diffusion halo assumed to be cylindrically symmetric, which extends a few kpc above and below the Galactic plane. In particular, it has a fixed radial extension of 20 kpc, while the half height of the diffusion halo is denoted by z_h and typically enters CRs fits as a free parameters (see section 2.4). When CRs cross the boundary of the diffusion halo they escape from the Galaxy, while the propagation within the halo is described by a chain of coupled diffusion equations.

The diffusion equation for the phase-space densities $\psi_i(\mathbf{x}, p, t)$ of CR species i at position \mathbf{x} and momentum p is given by [65]:

$$\begin{aligned} \frac{\partial \psi_i(\mathbf{x}, p, t)}{\partial t} = & q_i(\mathbf{x}, p) + \nabla \cdot (D_{xx} \nabla \psi_i - \mathbf{V} \psi_i) \\ & + \frac{\partial}{\partial p} p^2 D_{pp} \frac{\partial}{\partial p} \frac{1}{p^2} \psi_i - \frac{\partial}{\partial p} \left(\frac{dp}{dt} \psi_i - \frac{p}{3} (\nabla \cdot \mathbf{V}) \psi_i \right) - \frac{1}{\tau_{f,i}} \psi_i - \frac{1}{\tau_{r,i}} \psi_i. \end{aligned} \quad (2.3)$$

We briefly describe each of the terms in eq. (2.3) below. To solve these equations numerically we employ GALPROP 56.0.2870 [5, 66] and GALTOOLIBS 855³ with a few custom modification as described in [32]. Alternatively, solutions might be obtained analytically, utilizing various simplifying assumption [67, 68], or using other fully numerically codes like DRAGON [6, 69] or PICARD [70]. GALPROP assumes that CRs are in a steady state and solves the diffusion equations on a 3-dimensional grid. Two dimensions describe the spatial distribution of CRs, the radial distance r from the Galactic center and distance z perpendicular to the plane, and one dimension contains the CR's kinetic energy. The grid points of the spatial dimensions are spaced linearly with step size of $\Delta r = 1$ kpc and $\Delta z = 0.1$ kpc, respectively, while the grid is spaced logarithmically in kinetic energy with a ratio between successive grid points of 1.4.

The source term q_i in eq. 2.3 depends on the CR species. For secondary antiprotons and antiprotons from DM annihilation it takes the form of eq. (2.2) and eq. (2.1), respectively.

³<https://galprop.stanford.edu/download.php>

For primary CRs the source term factorizes into a spatial and a rigidity-dependent term. The spatial term traces the distribution of supernova remnants.⁴ On the other hand, the rigidity dependence is modeled as a smoothly broken power-law:

$$q_R(R) = \left(\frac{R}{R_0} \right)^{-\gamma_1} \left(\frac{R_0^{1/s} + R^{1/s}}{2 R_0^{1/s}} \right)^{-s(\gamma_2 - \gamma_1)}, \quad (2.4)$$

where R_0 is the break position and $\gamma_{1,i}$ and $\gamma_{2,i}$ are the spectral indices above and below the break, respectively. The parameter s regulates the amount of smoothing at the break. The broken power-law spectrum in Eq. 2.4 is a widely used phenomenological approximation which describes well the data in the considered rigidity range. All CR species are affected by several processes that contribute to CR propagation, which are diffusion, reacceleration, convection, and energy losses. We assume that diffusion is spatially homogeneous and isotropic. In this case, the diffusion coefficient, D_{xx} , can be modeled as a broken power-law in rigidity

$$D_{xx} = \begin{cases} \beta D_0 \left(\frac{R}{4 \text{GeV}} \right)^\delta & \text{if } R < R_1 \text{ and} \\ \beta D_0 \left(\frac{R_1}{4 \text{GeV}} \right)^\delta \left(\frac{R}{R_1} \right)^{\delta_h} & \text{otherwise,} \end{cases} \quad (2.5)$$

where D_0 is an overall normalization and δ and δ_h are the power-law indices below and above the break at position R_1 . At low energies the diffusion coefficient is proportional to the velocity $\beta = v/c$ of the CRs. We allow for a diffusive reacceleration of CRs by scattering off Alfvèn magnetic waves. The amount of reacceleration is then determined by the velocity v_{Alfven} of the waves [73, 74]:

$$D_{pp} = \frac{4 (p v_{\text{Alfven}})^2}{3(2-\delta)(2+\delta)(4-\delta) \delta D_{xx}}. \quad (2.6)$$

The terms proportional $\mathbf{V}(\mathbf{x})$ in eq. 2.3 describe convective winds which drive the CRs away from the Galactic plane. They are taken constant and orthogonal to the Galactic plane, such that $\mathbf{V}(\mathbf{x}) = \text{sign}(z) v_{0,c} \mathbf{e}_z$. The remaining terms describe different contributions of energy losses, for which we adopt the default GALPROP implementation. In particular, continuous energy losses like ionization or bremsstrahlung are included in the term dp/dt , while catastrophic energy losses by fragmentation or decay are modeled by the last two terms. The parameters τ_f and τ_r are the corresponding lifetimes.

We emphasize again that the setup of CR propagation described above reflects one specific choice. The available measurements of CR nuclei are also described well by other setups. In particular, a model without diffusive re-acceleration, but with an additional break in the diffusion coefficient between 5 and 10 GeV is currently discussed in the literature [54, 59, 64].

CRs measured at the top of the atmosphere have to traverse a significant part of the heliosphere where they are deflected and decelerated by solar winds. The strength of this effect varies in a 22-year cycle and is commonly known as solar modulation. It mostly affects

⁴We use the default prescription of GALPROP where the parameters of the source term distribution are fixed to $\alpha = 0.5$, $\beta = 2.2$, $r_s = 8.5$ kpc, and $z_0 = 0.2$ kpc. This is slightly different from recent values in the literature [71]. We note, however, that nuclei are only very weakly sensitive to the chosen distribution as discussed in Ref. [72].

low-energetic CRs; in practice the impact on the spectra above a few tens of GV is negligible. We use the common force-field approximation [75] to model the impact on the CR spectra:

$$\phi_{\oplus,i}(E_{\oplus,i}) = \frac{E_{\oplus,i}^2 - m_i^2}{E_{\text{LIS},i}^2 - m_i^2} \phi_{\text{LIS},i}(E_{\text{LIS},i}), \quad (2.7)$$

$$E_{\oplus,i} = E_{\text{LIS},i} - e|Z_i|\varphi_i. \quad (2.8)$$

Here Z_i is the charge number, e is the elementary charge, and φ_i is the solar modulation potential. The potential is known to be time and charge-sign dependent. The subscripts on the energy or flux denote the position which can either be local interstellar (LIS) or top of the atmosphere (\oplus). We note that the force-field approximation is probably an oversimplified treatment of solar modulation.⁵ To minimize systematic impacts from solar modulation on our results we will exclude data below 5 GV from our analysis. Furthermore, we allow a different solar modulation potential for antiprotons to account for a possible charge-sign dependence.

2.4 Fit to AMS-02 data

In the following we summarize very briefly the considered datasets and the fit strategies, where the latter are directly adopted from Ref. [32]. The most precise measurement of CR antiprotons above 1 GV is currently provided by the AMS-02 experiment [4]. We consider the data sets of proton, helium, and antiprotons from AMS-02 [4] collected over 7 years from 2011 to 2018 and complement with low-energy data for protons and helium from Voyager [81]. When fitting the CR data with the model outlined below, the CR likelihood is defined by

$$-2 \log \mathcal{L}_{\text{CR}}(\boldsymbol{\theta}) = \chi_{\text{CR}}^2(\boldsymbol{\theta}) = \sum_{e,s,i} \left(\frac{\phi_{s,i}^{(e)} - \phi_{s,i,e}^{(\text{m})}(\boldsymbol{\theta})}{\sigma_{s,i}^{(e)}} \right)^2. \quad (2.9)$$

where $\phi_{s,i}^{(e)}$ denotes the flux of the CR species s that was measured by the experiment e at the rigidity R_i or energy $E_{\text{kin},i}$, while $\phi_{s,i,e}^{(\text{m})}(\boldsymbol{\theta})$ is the flux computed with GALPROP for the corresponding species and energy. Finally, $\sigma_{s,i}^{(e)}$ is the experimental uncertainty of the flux measurement. The AMS-02 experiment provides separate statistical and systematic uncertainties. Here we assume that the systematic uncertainties are uncorrelated and add the two contribution in quadrature. This is certainly a simplified treatment. In particular, it was shown that the significance of a potential excess can depend critically on the assumptions made for the correlations of this uncertainty [33, 34]. However, we expect that the impact on DM limits is less severe. We leave the study of different systematics and correlations within the new methods introduced in this paper to future investigation.

Within the phenomenological description of CR injection and propagation outlined in Sec. 2.3, the parameters of eq. (2.3) are largely unconstrained a priori and are directly inferred from CR data. We allow for a total of 15 parameters to describe cosmic-ray injection and propagation. To sample this large parameter space efficiently we use the Nested Sampling algorithm implemented in the MULTINEST code [82]. The computing efficiency is increased even further by exploiting a hybrid strategy where only a subset of parameters is sampled by MULTINEST (“slow parameters”) and the remaining parameters are profiled on-the-fly (“fast

⁵In more sophisticated models solar modulation is described by propagation equations similar to eq. 2.3 but tuned to the environment of the heliosphere. These are typically solved numerically [76–80].

parameters”). The slow parameters are the ones that are needed as input for GALPROP and thus changing them is time consuming. More specifically, these are the following eleven parameters: the slopes of the primary injection spectra $\gamma_{1,p}$, γ_1 , $\gamma_{2,p}$, and γ_2 , the break position R_0 and its smoothing s , the normalization D_0 and slope δ of the diffusion coefficient, the half-height of the diffusion halo z_h , and the velocities of convection v_{0c} and Alfvén magnetic waves $v_{\text{Alfvén}}$. The scan ranges for all of these parameters are summarised in table 1.

The four remaining parameters describe the normalization of the proton (A_p) and helium (A_{He}) fluxes and the solar modulation potentials ($\varphi_{\text{AMS-02},p,\text{He}}$ for p and He and $\varphi_{\text{AMS-02},\bar{p}}$ for \bar{p}). These are the fast parameters, which are treated in a simplified way in our analysis and therefore can be varied much more easily. Instead of explicitly including them in the MULTINEST parameter scans, we profile over them on-the-fly at each likelihood evaluation of MULTINEST, i.e. we maximize the likelihood over the fast parameters using MINUIT [83]. A very weak Gaussian prior is applied to $\varphi_{\text{AMS-02},\bar{p}}$ by adding to the main likelihood the term $-2 \log(\mathcal{L}_{\text{SM}}) = (\varphi_{\text{AMS-02},p,\text{He}} - \varphi_{\text{AMS-02},\bar{p}})^2 / \sigma_\varphi^2$ where $\sigma_\varphi = 100$ MV, while no priors are applied on $\varphi_{\text{AMS-02},p,\text{He}}$.

We truncate the rigidity range of the fit to the range between 5 to 300 GV. As mentioned above, data below 5 GV is excluded to avoid a strong bias from our modeling of solar modulation.⁶ At high energies, the spectra of CR nuclei show a break at $R \sim 300$ GV, which is more pronounced in secondaries with respect to primaries [84, 85]. While in general it would be possible to introduce spectral breaks in the injection spectrum or in the diffusion coefficient, only the latter naturally explains the different behavior of the primaries and secondaries [86]. We therefore fix the parameters of eq. (2.5) to $R_1 = 300$ GV and $\delta_h = \delta - 0.12$. The proton and helium data of AMS-02 is described well by this choice. Truncating our fit at $R \sim 300$ GV avoids unnecessary bias.⁷

To gain a first understanding of the allowed regions of parameter space, we perform a CR fit as detailed above. The scan is conducted using 1000 live points, a stopping criterion of $\text{TOL}=0.1$ and an enlargement factor $\text{EFR}=0.7$. The final efficiency of the scan is found to be around 9%, with about 350 000 likelihood evaluations in total. The fit is heavily parallelized using 96 cores at the same time. The GALPROP code is parallelized using OPENMP while the nested sampling algorithm of MULTINEST can be expanded to multiple MPI tasks. We follow a hybrid strategy with 24 MPI tasks using 4 cores for each task. We have verified that the parallelization efficiency lies above 70%. In total the fit requires about 5.5 days to converge and consumes 12500 cpu hours, which means that a single likelihood evaluation requires on average about 130 cpu seconds. To perform this fit, MULTINEST starts by broadly sampling the entire parameter space and then continuously shrinks to the allowed parameters. The result is an ensemble of parameter points which is denser in the most interesting parameter region. We will make use of this property in the following section, where our goal is to train the ANNs in such a way that they perform particularly well in the parameter range preferred by data. Thus, we save all the sample points during the fit and then use them as a starting point for the training in section 3.

In table 1 we summarize the best-fit (most probable) values of the various parameters based on a frequentist (Bayesian) interpretation as well as their 68% confidence intervals (credible intervals). The best-fit point corresponds to $\chi^2 = 57.2$ for the AMS-02 data. These

⁶It was shown in Ref. [32] that the cut a $R = 5$ GV is not tuned to maximize a potential DM detection.

⁷As an alternative, R_1 and $\delta_h - \delta$ could be treated as free parameters in the fit which would, however, increase the complexity of the already high-dimensional parameter fit.

Table 1. Results of the CR fits to AMS-02 and Voyager data of protons, helium, and antiprotons. The parameter ranges for the MULTINEST scan are stated in column 2. In the remaining columns we state the best-fit parameter values and their uncertainty at the 68% C.L. for a fit with and without a DM signal. Results are given both in the frequentist and the Bayesian interpretation.

Parameter	Scan ranges	Frequentist		Bayesian	
		w/o DM	w/ DM	w/o DM	w/ DM
$\gamma_{1,p}$	[1.2, 2]	$1.80^{+0.04}_{-0.03}$	$1.79^{+0.07}_{-0.06}$	$1.77^{+0.07}_{-0.04}$	$1.68^{+0.14}_{-0.07}$
γ_1	[1.2, 2]	$1.79^{+0.04}_{-0.04}$	$1.74^{+0.08}_{-0.06}$	$1.75^{+0.07}_{-0.04}$	$1.63^{+0.15}_{-0.07}$
$\gamma_{2,p}$	[2.3, 2.6]	$2.405^{+0.013}_{-0.007}$	$2.48^{+0.02}_{-0.03}$	$2.41^{+0.01}_{-0.01}$	$2.48^{+0.02}_{-0.03}$
γ_2	[2.3, 2.6]	$2.357^{+0.014}_{-0.005}$	$2.42^{+0.02}_{-0.03}$	$2.366^{+0.009}_{-0.012}$	$2.42^{+0.02}_{-0.02}$
$R_0 [10^3 \text{ MV}]$	[1, 20]	$7.92^{+0.82}_{-0.80}$	$7.32^{+1.16}_{-0.83}$	$7.06^{+0.93}_{-1.04}$	$6.42^{+0.97}_{-1.13}$
s	[0.1, 0.9]	$0.37^{+0.03}_{-0.03}$	$0.40^{+0.03}_{-0.04}$	$0.38^{+0.04}_{-0.04}$	$0.44^{+0.04}_{-0.06}$
$D_0 [10^{28} \text{ cm}^2/\text{s}]$	[0.5, 10]	$2.05^{+1.48}_{-0.39}$	$2.92^{+2.09}_{-0.96}$	$3.58^{+1.30}_{-0.73}$	$5.37^{+1.52}_{-1.78}$
δ_l	[0.2, 0.6]	$0.419^{+0.009}_{-0.012}$	$0.35^{+0.03}_{-0.02}$	$0.42^{+0.01}_{-0.01}$	$0.33^{+0.03}_{-0.03}$
$v_{\text{Alfven}} [\text{km/s}]$	[0, 30]	$8.84^{+1.45}_{-2.58}$	$10.25^{+2.12}_{-2.06}$	$6.02^{+3.57}_{-2.51}$	$7.70^{+4.15}_{-3.10}$
$v_{0,c} [\text{km/s}]$	[0, 60]	$0.09^{+1.08}_{-0.08}$	$0.90^{+6.77}_{-0.78}$	$2.48^{+0.32}_{-2.48}$	$13.36^{+2.44}_{-13.36}$
$z_h [\text{kpc}]$	[2, 7]	$2.60^{+2.25}_{-0.48}$	$2.79^{+2.87}_{-0.75}$	$4.70^{+2.30}_{-0.86}$	$4.84^{+2.13}_{-0.75}$
$\log_{10}(m_{\text{DM}}/\text{MeV})$	[4, 7]	-	$5.07^{+0.03}_{-0.05}$	-	$5.08^{+0.04}_{-0.05}$
$\log_{10}(\langle \sigma v \rangle s/\text{cm}^3)$	[-27, -22]	-	$-25.42^{+0.22}_{-0.48}$	-	$-25.76^{+0.13}_{-0.26}$
$\varphi_{\text{AMS-02,pHe}} [\text{GV}]$		$0.26^{+0.04}_{-0.03}$	$0.25^{+0.05}_{-0.03}$	$0.30^{+0.04}_{-0.05}$	$0.28^{+0.04}_{-0.06}$
$(\varphi_{\bar{p}} - \varphi_p)_{\text{AMS-02}} [\text{GV}]$		$0.200^{+0.000}_{-0.036}$	$0.13^{+0.07}_{-0.12}$	$0.177^{+0.023}_{-0.001}$	$0.09^{+0.11}_{-0.03}$
$A_{p,\text{AMS-02}}$		$1.173^{+0.004}_{-0.003}$	$1.173^{+0.003}_{-0.004}$	$1.178^{+0.004}_{-0.004}$	$1.177^{+0.004}_{-0.004}$
$A_{\text{He},\text{AMS-02}}$		$1.257^{+0.006}_{-0.014}$	$1.20^{+0.02}_{-0.01}$	$1.253^{+0.010}_{-0.010}$	$1.20^{+0.02}_{-0.02}$
$\chi^2_{p,\text{AMS-02}}$		7.2	6.2		
$\chi^2_{\text{He},\text{AMS-02}}$		3.2	2.1		
$\chi^2_{\text{pbar/p,AMS-02}}$		35.0	21.5		
$\chi^2_{p,\text{Voyager}}$		7.9	4.1		
$\chi^2_{\text{He},\text{Voyager}}$		3.9	3.2		
χ^2		57.2	37.1		

results broadly agree with the ones from Ref. [32] even though we use the more recent 7-year AMS-02 data for p , He, and \bar{p} . As expected, for the parameters that are well-constrained by data, there is good agreement between the frequentist and the Bayesian approach. For less constrained parameters (such as for example z_h) there can be sizeable differences between the best-fit point (obtained by maximizing the profile likelihood) and the most probable point (obtained by maximizing the marginalized likelihood). We will return to this issue in section 4.

Previous analysis have discussed a potential DM signal that could be accommodated at

antiproton energies between 10 and 20 GeV where the antiproton flux shows a small anomaly at the level of a few percent. This potential signal corresponds, for example, to DM particles with a mass of about 80 GeV that self-annihilate into $b\bar{b}$ final states at a thermal cross section. However, the significance of this potential signal has been discussed controversially in the literature. The most recent works suggest that the anomaly is well explained by the combination of several systematic uncertainties, namely uncertainties in the secondary antiproton production cross section, correlated systematics in the AMS-02 data, and some additional freedom in the CR propagation model [33–35], which we do not include here.

The focus of this work lies instead on developing new methods for exploiting ANNs and importance sampling to derive DM limits. In contrast to a DM signal, we expect the limits to be only weakly dependent on those systematics and leave their investigation to future studies. Nevertheless, for comparison we also perform one fit where antiprotons from DM annihilation are included. We choose DM annihilation into a pair of $b\bar{b}$ quarks as our benchmark. In this case, two further parameters are considered, the mass of the DM particle m_{DM} and the thermally averaged annihilation cross section $\langle\sigma v\rangle$ (see eq. 2.2). We explore values of m_{DM} from 10 GeV to 10 TeV and values of $\langle\sigma v\rangle$ between 10^{-22} and 10^{-27} cm³/s, with our results being independent of the precise choice of these ranges. These two additional parameters are sampled with MULTINEST.

The results of the additional fit are also shown in table 1. Including a DM signal formally improves the χ^2 by 20.1 which, however, given the discussion above should not be interpreted as significant. Nonetheless, we can take this value as a point of comparison for the performance of the ANN in section 4. Finally, we highlight a further important observation. The additional DM signal affects the CR propagation parameters only marginally which implies that we can use the sample of propagation parameters obtained from the CR fit described above irrespective of the precise DM parameters for the training of the ANN (see section 3) and for the statistical inference via importance sampling (see section 4).

In the previous paragraph, we focussed on a specific case of DM annihilation into a pair of bottom quarks which serves as an example and a point of comparison. In general, much more complex scenarios with a range of different final states and combinations at different branching fraction are possible. The naive approach to obtain results would be to perform an entirely new parameter scan for each case of interest which obviously requires a substantial amount of computational resources. Instead, in the following we will discuss methods to speed up the calculation of CR spectra in a model-independent fashion to quickly obtain constraints for any given DM model.

3 Deep Neural Network Setup and Training

Our aim is to predict the output of GALPROP for a wide range of input parameters representing both uncertainties in the propagation model and the unknown properties of DM. This output can then be used to calculate experimental likelihoods as described in section 2.4 without computationally expensive simulations. To achieve this goal, we build and train suitable ANNs and validate their performance. Considering the two different contributions to the antiproton flux (i.e. primary and secondary CRs), we construct two separate ANNs to provide fast predictions of each component based on the relevant physical parameters. We will refer to the networks for the DM component and the secondary component as DMNet and sNet, respectively. As the underlying method in the development of the neural networks is the same, both ANNs will be presented in parallel in this section.

3.1 Training Set

The information that a neural network should be able to learn, in general, has to be represented in the data that is used to train the network. This allows for the interpolation of data within the parameter space that would, in a conventional approach, require new simulations. To remain impartial on the specific parameters of the DM model, we consider a wide range in the mass of the DM particle from 5 GeV to 5 TeV and randomly sample from a logarithmic distribution in this range. A similar approach is taken for the branching fractions, where we consider all SM final states that give a non-negligible contribution to a CR antiproton flux [36]: $q\bar{q}$, $c\bar{c}$, $b\bar{b}$, $t\bar{t}$, W^+W^- , ZZ , hh and gg . We logarithmically sample each branching fractions in the range $[10^{-5}, 1]$ and then normalise the result in such a way that the sum of all branching fractions equals one. The DM annihilation cross section is fixed to $\langle\sigma v\rangle = 3 \times 10^{-26} \text{ cm}^3 \text{ s}^{-1}$ in the complete training set, as variations in this parameter can be included at a later stage by an appropriate rescaling of the flux. These DM parameters, which we will collectively denote by \mathbf{x}_{DM} , are only relevant to the DM component of the antiproton flux and the corresponding neural network, while the secondary flux is independent of \mathbf{x}_{DM} and hence these parameters will not be used as inputs to the sNet.

For the propagation parameters we face the significant challenge that the parameter space introduced in section 2 is 11-dimensional and that only a very small volume of this parameter space gives an acceptable fit to AMS-02 data. If we were to simply perform a grid scan or draw random samples from this parameter space, we would include large regions of parameter space for which accurate predictions are unnecessary, as they will anyways be strongly excluded. Conversely, in the preferred regions of parameter space, we want to achieve an accuracy that is significantly better than the typical relative errors of about 5% in AMS-02 data, which requires large amounts of training data.

To obtain sufficiently accurate network predictions in the most interesting regions of parameter space without spending unnecessary time on the simulation and training of less interesting regions, we want to make use of the AMS-02 data already for the creation of the training set. Indeed, we can directly use the MULTINEST scan described in section 2.4 to obtain a sample of propagation parameters (denoted by $\boldsymbol{\theta}_{\text{prop}}$ in the following) that is focused on the regions of parameter space with the highest likelihood (see also Ref. [87]). For the creation of the training set we exclude any parameter point in the MULTINEST sample that gives a poor fit to AMS-02 data, specifically with $\Delta\chi^2 \geq 30$ compared to the best-fit point. This results in a total of 117335 remaining parameter points which we show in figure 1. We emphasize that for each parameter the training data extends well beyond the 68% confidence/credible intervals quoted in table 1 and covers the preferred parameter regions both with and without DM annihilations. To ensure a sufficiently good coverage also of the DM parameter space, we sample 8 sets of DM parameters for each propagation parameter set leading to a very large simulation set of $\mathcal{O}(10^6)$ parameter points.

3.2 Neural Network Architectures

Although the two networks that we use to predict the two components of the antiproton flux can be set up and trained in a similar way, we face distinct challenges in each component. For the DMNet the key challenge is the very large number of input parameters, namely the DM mass plus 8 branching fractions in \mathbf{x}_{DM} and a total of 11 propagation parameters in $\boldsymbol{\theta}_{\text{prop}}$, each with a different physical effect on the output, i.e. the antiproton flux. As we want to have accurate predictions for variations in each of the parameters, we treat the DM mass, the branching fractions, and the propagation parameters as three distinct sets of inputs, which

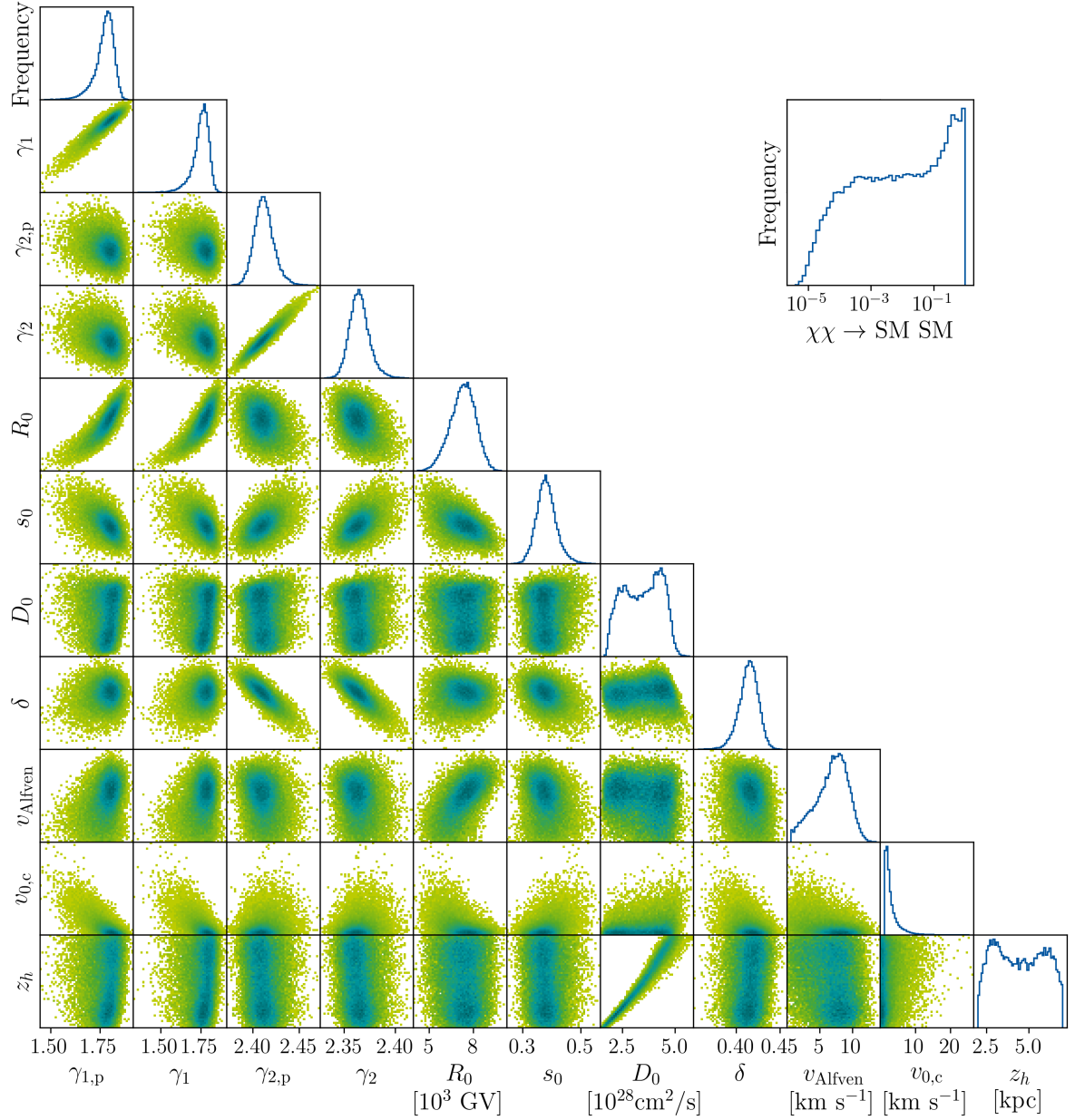


Figure 1. *Triangle plot:* One and two dimensional histograms of propagation parameters used in the training set, constructed in such a way that the highest density is achieved in the regions most favoured by the combination of AMS-02 proton, antiproton and helium data without DM signal. *Top right:* One dimensional histogram of the training set for each of the branching fractions $\chi\chi \rightarrow \text{SM}$.

are first processed by three independent dense networks before combining the outputs (see below).

For the sNet the key challenge is to achieve sufficient accuracy in the prediction of the secondary antiprotons flux, which is tightly constrained by AMS-02 data. Given these constraints, the secondary antiproton flux only exhibits relatively small variations across the training set, which nevertheless need to be accurately captured using the sNet. To achieve

the desired accuracy, we provide an increased number of trainable parameters that define the network. As we will show within the following sections, the training duration consequently increases with respect to the DMNet but a very good accuracy is achieved.

Rather than directly feeding the physical parameters as inputs to the network, we map the logarithm of \mathbf{x}_{DM} to values in the range $[0, 1]$ and the remaining parameters $\boldsymbol{\theta}_{\text{prop}}$ to a distribution with a mean of 0 and a standard deviation of 1. Each of the networks is then trained in a supervised approach. The simulated fluxes serve as training labels or ‘true’ fluxes to which the network output can be compared.

Given the large variations in the CR fluxes that are desired as the output of the ANNs, here we choose a natural scaling of the original (simulated) flux $\Phi(E)$ for the sNet outputs,

$$\tilde{\Phi}_s(E) = \log_{10} (\Phi(E) E^{2.7}) . \quad (3.1)$$

The \log_{10} further decreases the variations in the flux values, which would otherwise cover several orders of magnitude. The energies and their respective fluxes are binned values, identical to the output from the simulations, which extend over the energy range of the AMS-02 antiproton measurement. Consequently, we have sequences of distinct values in the scaled flux as training labels. The transformation in eq. (3.1) is easily invertible and thus allows for direct comparison of the network output to the simulated spectra.

As the DM component of the flux predominantly scales with the DM mass, we choose a different scaling for that flux component,

$$\tilde{\Phi}_{\text{DM}}(E) = \log_{10} (m_{\text{DM}}^3 x \Phi(E)) , \quad (3.2)$$

where $x = E/m_{\text{DM}}$ is a dimensionless quantity. We fix a grid in x on which we evaluate the training labels and DMNet output. The advantage of this scaling compared to eq. (3.1) is that it substantially reduces the impact of changing the DM mass and therefore leads to much less variation across the training set.⁸ This is illustrated in Fig. 2, which shows the resulting DM antiproton fluxes $\tilde{\Phi}_{\text{DM}}$ as a function of x for a representative set of final state combinations and DM masses in the training set. We find that for each set of input parameters we obtain a slowly-varying function of x that reaches a maximum and then drops towards $x \rightarrow 1$. The general trend is similar across the entire range of DM masses that we consider, but some information on the DM mass is retained. We find that this approach significantly improves the training of the DMNet compared to the scaling in eq. (3.1).

Subsequent to the pre-processing of the input, the ANNs contain densely connected (‘dense’) layers, that process the information from the inputs. To address the individual challenges for the networks we set up the architecture as depicted in figure 3. We provide dense layers for each of the different inputs in the DMNet which are concatenated in the next step and followed by large dense layers. In the sNet the pre-processed input is fed through a more intricate set of dense layer, specifically (56, 28, 14, 28, 56) nodes in the set of layers. We use ReLU activations and add a small dropout probability of 0.1% between the layers.

The main feature of each of the networks is a recurrent layer. The choice to work with a recurrent setup instead of other network architecture types has lead to significant improvements in the architecture development process. Even though the typical application for RNNs is time-series data, we find our spectra as functions of energy to be handled just as well by this network type. In particular, it can be reasoned that the information

⁸To first approximation the DM component of the antiproton flux follows the source term $\Phi_{\bar{p},\text{DM}}(E) \propto q_{\text{DM}} \propto m_{\text{DM}}^{-2} dN/dE \propto m_{\text{DM}}^{-3} x^{-1} dN/d\log_{10} x$, where $dN/d\log_{10} x$ depends only very mildly on m_{DM} .

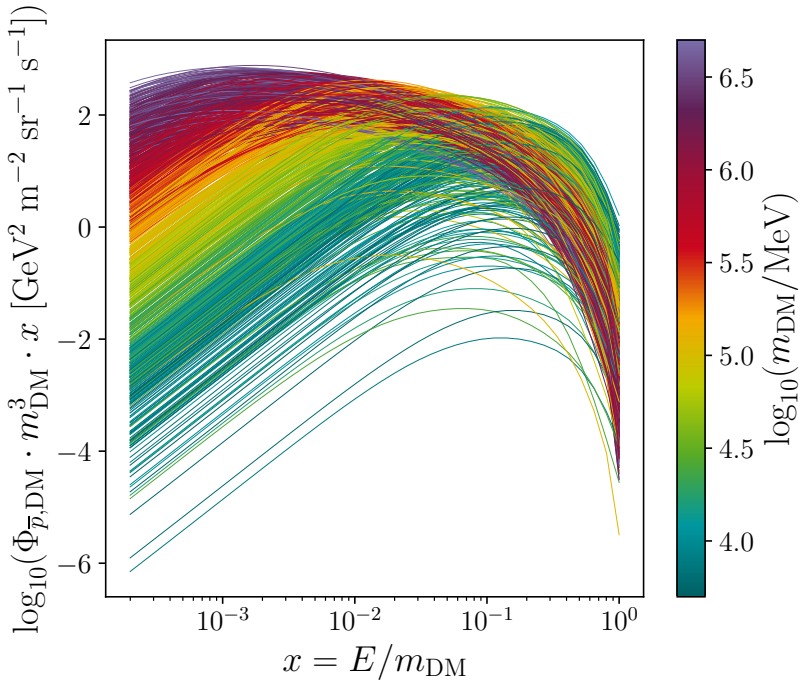


Figure 2. Transformed DM antiproton fluxes following eq. 3.2 for our training set, which varies propagation parameters, branching fractions and DM masses as discussed in sec. 3.1. The modest amount of variation across different parameter points results in a more easily processable version of the input GALPROP simulated flux for the DMNet.

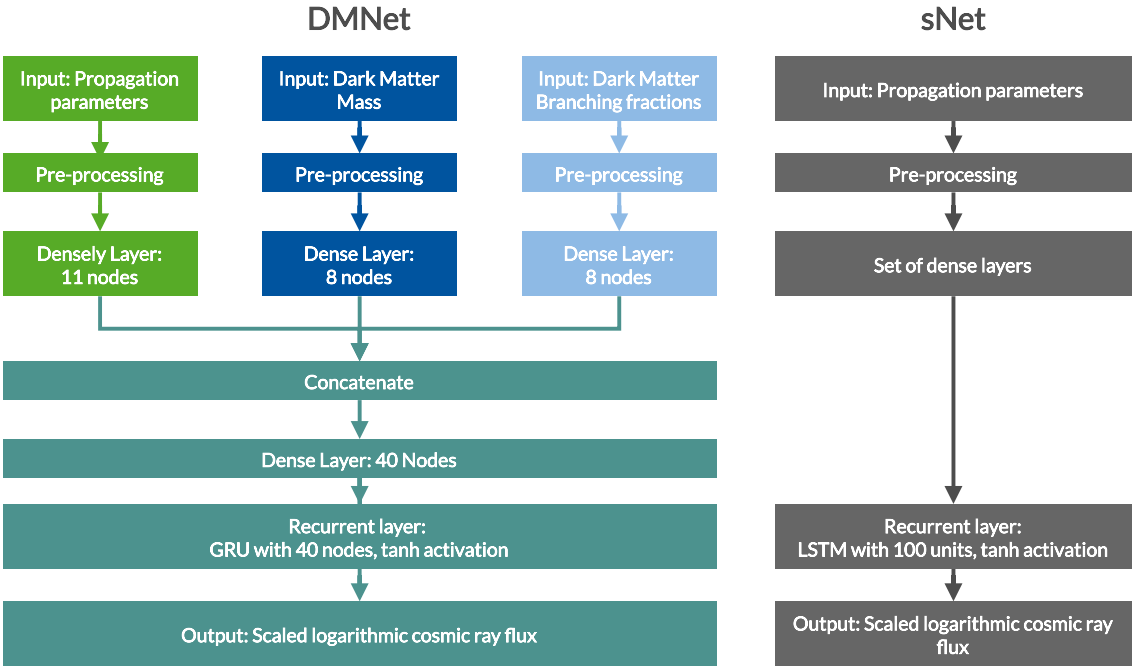
on the flux that is contained in a specific energy bin is highly correlated with the prior and subsequent energy bins and a network architecture that is able to propagate the information of neighbouring units is very beneficial for the task at hand. We chose a GRU layer as proposed in [88] in the DMNet and a LSTM layer following [89] in the sNet. Each of these layer types is useful for long data sequences and far-reaching information propagation without leading to vanishing or exploding gradients during training. While both methods can in principle be used for either networks, the final implementations that achieved the best results was based on different layer types. As network output a final dense layer is set up. We build the networks using the deep learning API KERAS [90] which uses TENSORFLOW [91] as backend.

3.3 Training process

We use approximately 75% of the previously described simulation set for the network training.⁹ The remainder is used as a test set on which network performance evaluations can be conducted. Within the training set, a validation split of 20% is used during training to monitor the generalization capabilities of the network. Unlike the training loss, the loss calculated on the validation set is not used to update the model parameters during the optimization process.

The network training was conducted using the ADAM optimizer [92] and a mean squared error (MSE) loss. The initial learning rate of 10^{-2} is decreased during the training process,

⁹Note that the sNet has a smaller training set compared to the DMNet, as here we have fewer unique spectra following from our parameter sampling for simulating the training set.



Hyperparameters

Activation	ReLU
Dropout fraction	0.1 %
Optimizer	Adam, learning rate scheduling $l \in [10^{-2}, 10^{-5}]$, patience 10 epochs
Loss	Mean squared error (MSE)
Batch size	500
Validation split	20 %
Early stopping	Monitor val. loss, patience = 40

Figure 3. Schematic of the network structure. *Top left:* Architecture set up for handling the complete set of inputs. This network type can be used to be trained on the DM component of the \bar{p} flux (DMNet). *Top right:* Simplified architecture for networks that require only the CR propagation parameters as input. This network architecture is designed for learning the $\bar{p}_{\text{secondary}}$ fluxes (sNet) and can be employed to train on proton and helium spectra as well (see A). *Bottom:* The hyperparameter used during the training process for each of these networks.

based on the behaviour of the validation loss, for a optimal convergence to a minimal loss. After the learning rate reaches its predefined minimum ($lr = 10^{-5}$) the training process is terminated after 40 epochs without improvement of the validation loss, using an early stopping mechanism. This process helps ensure the convergence of the network optimization. The MSE loss for both the training and validation loss over the training epochs is shown in Fig. 4 for both ANNs.

We performed the training on a V100-SXM2 GPU. Given the depth of the individual

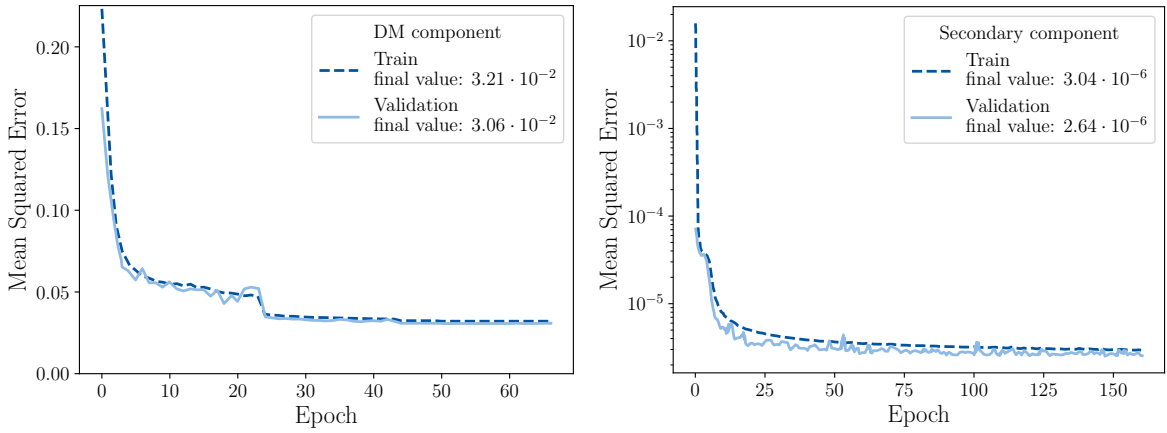


Figure 4. Evolution of the MSE loss for the neural networks trained on the DM component (*left*) and secondary component (*right*) of the antiproton flux over the training epochs.

networks, this resulted in training durations of about 4 minutes per epoch of the DMNet and about 12 minutes per epoch for the sNet.

3.4 Validation of the Network Performance

Training performance measures, such as the loss based on the training set, can be helpful while adjusting the architecture and hyperparameters of the networks. The usage of the networks however, requires an evaluation of their ability to replace the simulations. Using the fully trained networks we can compare the simulated spectra from GALPROP within the test set to the network predictions based on the same parameter sets. An example for such a comparison is shown in figure 5. We show the simulated spectra and the output of the respective ANNs for both the secondary and DM component of the antiproton flux (as well as for their sum). In the top panel we depict the fluxes in physical space alongside the AMS-02 antiproton data, demonstrating that the network provides fluxes that are extremely similar to the corresponding simulations. This is illustrated even more clearly in the bottom panel, which shows the relative differences between the ANN and the simulation with respect to the simulated total antiproton flux, compared to the relative uncertainties of the AMS-02 antiproton data. The parameter point for the specific example presented in figure 5 was randomly selected from the extensive test set.

We conclude that the accuracy of the sNet is fully sufficient: the relative difference between the fluxes predicted by the ANN and the simulated GALPROP fluxes are always well below the relative uncertainty of the AMS-02 measurements. The architecture and training process used for the sNet can analogously be applied to train an ANN on proton and Helium spectra based on the same GALPROP simulation set, achieving a comparable accuracy. We provide additional details on these networks in appendix A.

Given that the DMNet is trained on a parameter space of much higher dimensionality, it is unsurprising that its predictions are on average less accurate than the ones of the sNet. Indeed when calculating the relative differences between simulations and network predictions for the DM component only, we find that only 72% of samples lie on average within the AMS-02 relative uncertainties. However, it is essential to realize that in any realistic setting the DM component will only constitute a subdominant contribution to the antiproton flux. Indeed, if the DM contribution in a given bin significantly exceeds the

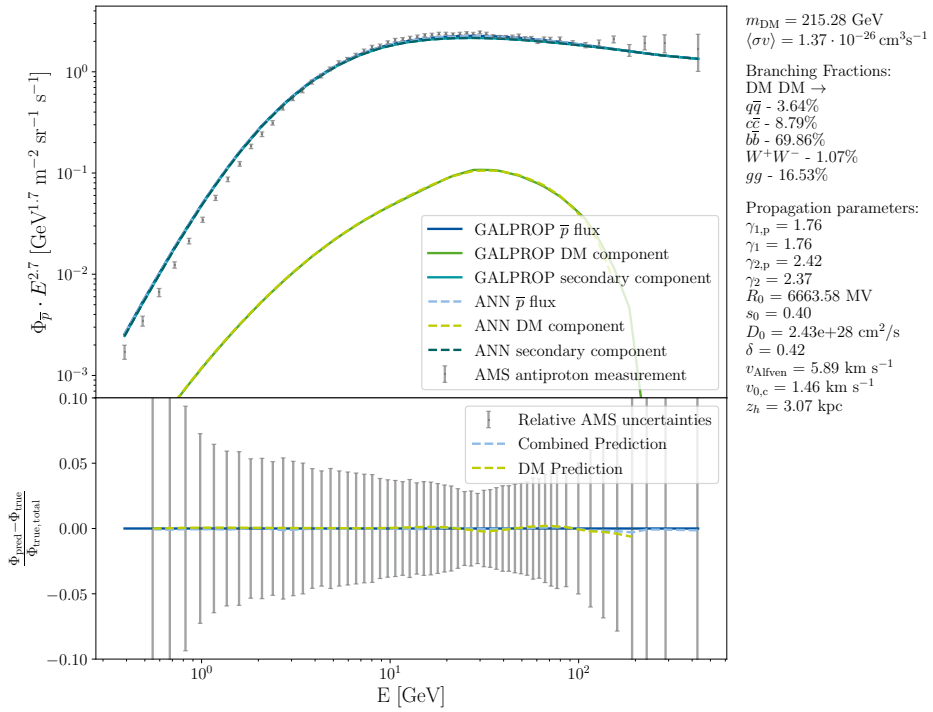


Figure 5. Exemplary comparison of the simulated vs predicted antiprotons flux of only the DM component and the combination of secondary and DM component where the listed parameters and simulated fluxes are randomly sampled from the test set. Each component of the neural network flux is predicted by the individual networks. The lower panel depicts the relative difference between the simulated and predicted fluxes with respect to the simulated flux compared to the relative AMS-02 uncertainty.

uncertainty of the AMS-02 data (which is typically at the level of 5%) the model is expected to be excluded.

In order to provide more realistic estimates of the general accuracy and stability of the DMNet performance within the test set, we therefore focus on DM signals that contribute 5% to the total antiproton flux in the bin where the relative DM contribution is largest. We then calculate the differences between simulations and network output relative to the total antiproton flux. This approach shows that even if the DMNet itself is only accurate at the level of 10%, the total antiproton flux can still be predicted with an accuracy at the sub-percent level for allowed DM models.

In figure 6, we show this accuracy estimate for a total of 3000 DM component samples from the test set (1000 samples each for three different mass bins corresponding to the three different rows). Here we compute the deviation between DMNet prediction and simulation to the corresponding total antiproton flux, as in the lower panel of figure 5. Since the deviations are found to be minuscule when compared to the AMS-02 relative uncertainties, we provide in the right column of figure 6 a zoomed-in version. It can be seen that the uncertainty bands (containing the central 68% of the network predictions) are typically at the level of 0.1% and do not exhibit any systematic shifts nor any significant dependence on the DM mass.

In the following we will be interested in comparing the total antiproton flux to data in order to determine which DM signals are allowed by observations. The comparison between

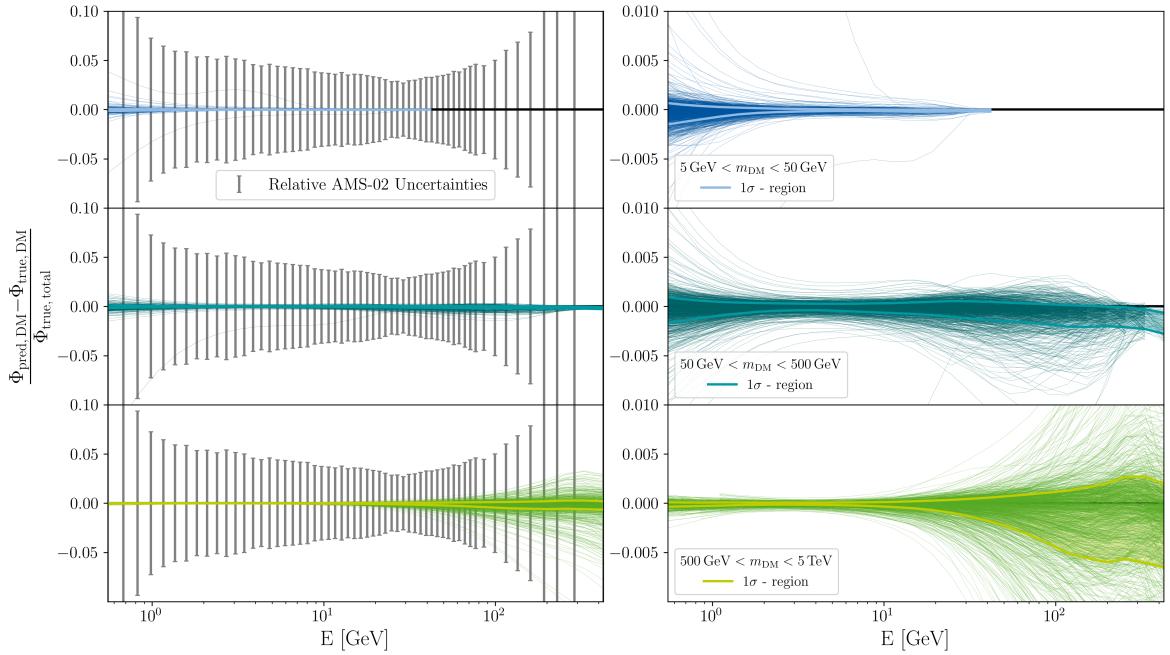


Figure 6. Relative deviations between predicted and simulated fluxes for the DM component binned into three mass bins and their 68 percentile. Each of the panel shows 1000 samples from the test set. As in the lower panels in Fig. 5, we again compare this to the benchmark of the relative AMS-02 uncertainties.

the network accuracy and the AMS-02 uncertainties in figure 6 clearly shows that it is fully sufficient for this purpose to use the ANNs instead of running GALPROP. Indeed, we will show explicitly in the next section that both approaches lead to very similar values for the χ^2 statistic described in section 2.4.

4 Constraining the Dark Matter Annihilation Cross Section

4.1 Statistical method

The ANNs described in the previous section enable us to obtain predictions of the primary and secondary anti-proton flux as a function of the DM parameters \mathbf{x}_{DM} and the propagation parameters $\boldsymbol{\theta}_{\text{prop}}$. Given data from observations we can then construct a likelihood function $\mathcal{L}(\mathbf{x}_{\text{DM}}, \boldsymbol{\theta}_{\text{prop}})$. We emphasize that, given suitable predictions for the CR fluxes, this likelihood is quick to evaluate and therefore does not need to be predicted by the ANN. This has the significant advantage that the ANN does not need to learn the various fluctuations that may be present in the data.

The likelihood function can then be used to constrain both \mathbf{x}_{DM} and $\boldsymbol{\theta}_{\text{prop}}$. In the present work we primarily focus on the constraints on the DM parameter space, meaning that we will treat the propagation parameters simply as nuisance parameters that need to be varied in order to draw robust conclusions. The two main ways to achieve this is to either calculate the profile likelihood

$$\hat{\mathcal{L}}(\mathbf{x}_{\text{DM}}) = \mathcal{L}(\mathbf{x}_{\text{DM}}, \boldsymbol{\theta}_{\text{prop}}(\mathbf{x}_{\text{DM}})) , \quad (4.1)$$

where $\hat{\boldsymbol{\theta}}_{\text{prop}}(\mathbf{x}_{\text{DM}})$ denote the propagation parameters that maximize the likelihood for given DM parameters \mathbf{x}_{DM} , or to calculate the marginalised likelihood

$$\bar{\mathcal{L}}(\mathbf{x}_{\text{DM}}) = \int \mathcal{L}(\mathbf{x}_{\text{DM}}, \boldsymbol{\theta}_{\text{prop}}) p(\boldsymbol{\theta}_{\text{prop}}) d\boldsymbol{\theta}_{\text{prop}} , \quad (4.2)$$

where $p(\boldsymbol{\theta}_{\text{prop}})$ denotes the prior probability for the propagation parameters. Given sufficiently constraining data, the profile likelihood and the marginalised likelihood are expected to be similar and the dependence of the result on the chosen priors should be small. We find that this is largely true for the case considered here, with some notable exceptions to be discussed below.

From the point of view of our machine learning approach, however, the two ways of varying the nuisance parameters are very different. The profile likelihood depends only on the anti-proton flux for a single value of $\boldsymbol{\theta}_{\text{prop}}$, meaning that highly accurate predictions are needed close to the maximum of the likelihood. For extreme choices of the DM parameters this maximum may be pushed to corners of parameter space where the network has not been sufficiently trained. A single outlier in the prediction will then completely bias the result and lead to numerical instabilities. This makes accurate calculations of the profile likelihood a highly challenging task.

The marginalised likelihood, on the other hand, depends on the likelihood across a range of propagation parameters, which should have substantial overlap with the parameter regions seen during training. The impact of individual outliers in the predictions is also reduced significantly compared to the case of the profile likelihood, making the calculation of marginalised likelihoods based on ANN predictions more robust. Nevertheless, the challenge remains to ensure that results are not biased by regions of parameter space where only little training has been performed. In the present work we address this challenge using the technique of importance sampling [93], which we describe in the following.

First of all, we note that an approximate marginalization can be performed by drawing a random sample of parameter points $\boldsymbol{\theta}_i$ from the prior probability $p(\boldsymbol{\theta}_{\text{prop}})$ and calculating the sum

$$\bar{\mathcal{L}}(\mathbf{x}_{\text{DM}}) \approx \frac{1}{N} \sum_{i=1}^N \mathcal{L}(\mathbf{x}_{\text{DM}}, \boldsymbol{\theta}_i) . \quad (4.3)$$

In fact, the same can be done by drawing a random sample from any probability distribution function $q(\boldsymbol{\theta}_{\text{prop}})$ provided the individual points are reweighted accordingly (so-called importance sampling):

$$\bar{\mathcal{L}}(\mathbf{x}_{\text{DM}}) \approx \frac{\sum_{i=1}^N \mathcal{L}(\mathbf{x}_{\text{DM}}, \boldsymbol{\theta}_i) \frac{p(\boldsymbol{\theta}_i)}{q(\boldsymbol{\theta}_i)}}{\sum_{i=1}^N \frac{p(\boldsymbol{\theta}_i)}{q(\boldsymbol{\theta}_i)}} . \quad (4.4)$$

A particularly interesting case is that $q(\boldsymbol{\theta}_{\text{prop}})$ is taken to be the posterior probability for the propagation parameters in the absence of a DM signal, i.e.

$$q(\boldsymbol{\theta}_{\text{prop}}) \propto \mathcal{L}(\mathbf{x}_{\text{DM}} = 0, \boldsymbol{\theta}_{\text{prop}}) p(\boldsymbol{\theta}_{\text{prop}}) \equiv \mathcal{L}_0(\boldsymbol{\theta}_{\text{prop}}) p(\boldsymbol{\theta}_{\text{prop}}) . \quad (4.5)$$

In this case $p(\boldsymbol{\theta}_i)/q(\boldsymbol{\theta}_i) \propto 1/\mathcal{L}_0(\boldsymbol{\theta}_i)$ and hence

$$\bar{\mathcal{L}}(\mathbf{x}_{\text{DM}}) \approx \frac{\sum_{i=1}^N \frac{\mathcal{L}(\mathbf{x}_{\text{DM}}, \boldsymbol{\theta}_i)}{\mathcal{L}_0(\boldsymbol{\theta}_i)}}{\sum_{i=1}^N \frac{1}{\mathcal{L}_0(\boldsymbol{\theta}_i)}} . \quad (4.6)$$

The great advantage of this approach is that the likelihood is only evaluated for plausible values of the propagation parameters, meaning for values that give a large posterior probability in the absence of a DM signal. These are exactly the same parameter regions on which we have focused for the training of the ANNs described above. Indeed, it is possible to generate the training data and sample the posterior probability using the same prior probabilities and the same MULTINEST runs such that a large overlap between the two is ensured.¹⁰ Another significant advantage is that it is straight-forward to include additional constraints on the propagation parameters that are independent of the DM parameters and therefore not part of the ANN training. For example, to also include likelihoods for proton data \mathcal{L}_p and He data \mathcal{L}_{He} , it is sufficient to draw a sample from the joint posterior

$$q(\boldsymbol{\theta}_{\text{prop}}) \propto \mathcal{L}_0(\boldsymbol{\theta}_{\text{prop}}) \mathcal{L}_p(\boldsymbol{\theta}_{\text{prop}}) \mathcal{L}_{\text{He}}(\boldsymbol{\theta}_{\text{prop}}) p(\boldsymbol{\theta}_{\text{prop}}). \quad (4.7)$$

To conclude this discussion, we note that in the case that the likelihood can be written in terms of a χ^2 function, $\mathcal{L} \propto e^{-\chi^2/2}$, we can define a marginalised χ^2 function as $\bar{\chi}^2(\mathbf{x}_{\text{DM}}) \equiv -2 \log \bar{\mathcal{L}}(\mathbf{x}_{\text{DM}})$. Importance sampling then yields

$$\bar{\chi}^2(\mathbf{x}_{\text{DM}}) = -2 \log \frac{\sum_{i=1}^N \exp\left(-\frac{\Delta\chi^2(\mathbf{x}_{\text{DM}}, \boldsymbol{\theta}_{\text{prop}})}{2}\right)}{\sum_{i=1}^N \exp\left(\frac{\chi_0^2(\boldsymbol{\theta}_{\text{prop}})}{2}\right)}, \quad (4.8)$$

where $\chi_0^2(\boldsymbol{\theta}_{\text{prop}}) = \chi^2(\mathbf{x}_{\text{DM}} = 0, \boldsymbol{\theta}_{\text{prop}})$ and $\Delta\chi^2(\mathbf{x}_{\text{DM}}, \boldsymbol{\theta}_{\text{prop}}) = \chi^2(\mathbf{x}_{\text{DM}}, \boldsymbol{\theta}_{\text{prop}}) - \chi_0^2(\boldsymbol{\theta}_{\text{prop}})$. To calculate confidence intervals and exclusion limits for the DM parameters, we then define

$$\Delta\bar{\chi}^2(\mathbf{x}_{\text{DM}}) = \bar{\chi}^2(\mathbf{x}_{\text{DM}}) - \bar{\chi}_0^2. \quad (4.9)$$

Hence, $\Delta\bar{\chi}^2 < 0$ corresponds to a preference for a DM signal, while parameter points with $\Delta\bar{\chi}^2 > 3.84$ can be excluded at 95% confidence level.¹¹

4.2 Example A: Single Dark Matter Annihilation Channel

Let us first consider a frequently-used benchmark scenario and assume that the DM particles annihilate exclusively into pairs of bottom quarks, such that the injection spectrum is fully characterised by the (velocity-independent) annihilation cross section $\langle\sigma v\rangle$ and the DM mass m_{DM} . As a first step, we can then calculate $\Delta\chi^2(m_{\text{DM}}, \langle\sigma v\rangle, \boldsymbol{\theta}_{\text{prop}})$ for different values of the propagation parameters. Figure 7 compares the results that we obtain when using the ANN predictions of the antiproton flux and when employing GALPROP. The two panels correspond to different values of the DM mass and use the same 10122 sets of propagation parameters drawn randomly from the posterior distribution $q(\boldsymbol{\theta}_{\text{prop}})$ as discussed above. In both cases we find a very strong correlation between the two ways of calculating $\Delta\chi^2$ ($r > 0.98$). Indeed, for 95% of parameter points the absolute difference in $\Delta\chi^2$ is smaller than 2.1 (0.9) for $m_{\text{DM}} = 100 \text{ GeV}$ ($m_{\text{DM}} = 1 \text{ TeV}$), confirming the excellent performance of our ANN.

In each case we use a dashed line to indicate $\Delta\bar{\chi}^2$ as defined in eq. (4.8). We emphasize that, since we average over $\exp(-\Delta\chi^2/2)$, the final result is dominated by the points with the smallest $\Delta\chi^2$. Again, we find very good agreement between the marginalised $\Delta\chi^2$ obtained

¹⁰We emphasize that the posterior sample is not part of the training data, i.e. the ANN is never evaluated on the exact same values seen during training.

¹¹Note that although our treatment of nuisance parameters is motivated by Bayesian statistics, we still interpret the resulting marginalized likelihood using frequentist methods, such that there is no need to choose priors for the DM parameters.

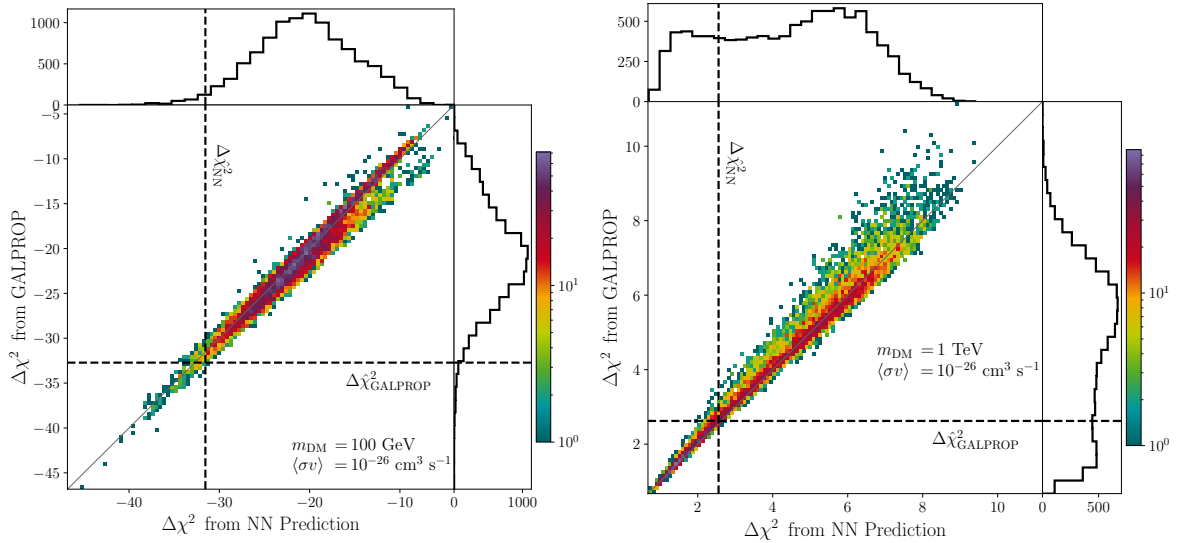


Figure 7. One and two dimensional histograms of $\Delta\chi^2$ for the AMS-02 antiproton measurement based on the antiproton fluxes provided by the Neural Network and GALPROP for different combinations of propagation parameters. We consider the annihilations of DM particles with $m_{\text{DM}} = 100 \text{ GeV}$ (left) and 1 TeV (right) into $b\bar{b}$ with a cross section of $\langle\sigma v\rangle = 10^{-26} \text{ cm}^3 \text{ s}^{-1}$. The values for $\Delta\chi^2$ indicated by the black dashed lines represent the marginalised values obtained by the importance sampling technique described in Section 4.1.

from the ANN and from GALPROP. The values obtained in the left panel correspond to a substantial preference for a DM signal, while the parameter point considered in the right panel is slightly disfavoured by data. Although the value $\Delta\chi^2 = -31.5$ (-32.7) that we obtain for $m_{\text{DM}} = 100 \text{ GeV}$ from the ANN (GALPROP) would at face value correspond to quite a significant excess, we caution the reader that due to our simplified implementation of AMS-02 data (in particular neglecting correlations) this number should be interpreted with care. We expect that a more detailed analysis of AMS-02 data would lead to a much lower significance.

A complementary perspective is provided in figure 8, which shows $\Delta\chi^2$ as a function of $\langle\sigma v\rangle$ for different values of the DM mass. In the left panel we fix the propagation parameters to their best-fit values in the absence of a DM signal (see table 1), while in the right panel we marginalise over all propagation parameters using importance sampling. Solid (dotted) curves correspond to the ANN (GALPROP) predictions and again show excellent agreement. The horizontal dashed lines indicate the 95% confidence level upper bound on $\langle\sigma v\rangle$ obtained following eq. (4.9).

As expected, allowing variations in the propagation parameters generally leads to smaller values of $\Delta\chi^2$ and hence relaxes the upper bounds on the annihilation cross section. This effect is most dramatic for the case $m_{\text{DM}} = 100 \text{ GeV}$ (blue line), where there is a preference for a DM signal in the data and hence the exclusion limit is relaxed by about an order of magnitude. The small bumps in the blue curve in the right panel are a result of the finite size of the sample of propagation parameters used for the marginalisation and result from the approximation made in eq. (4.4).

Repeating this procedure for different values of the DM mass, we can obtain exclusion limits on $\langle\sigma v\rangle$ as a function of m_{DM} . These are shown in figure 9 for the case of fixed

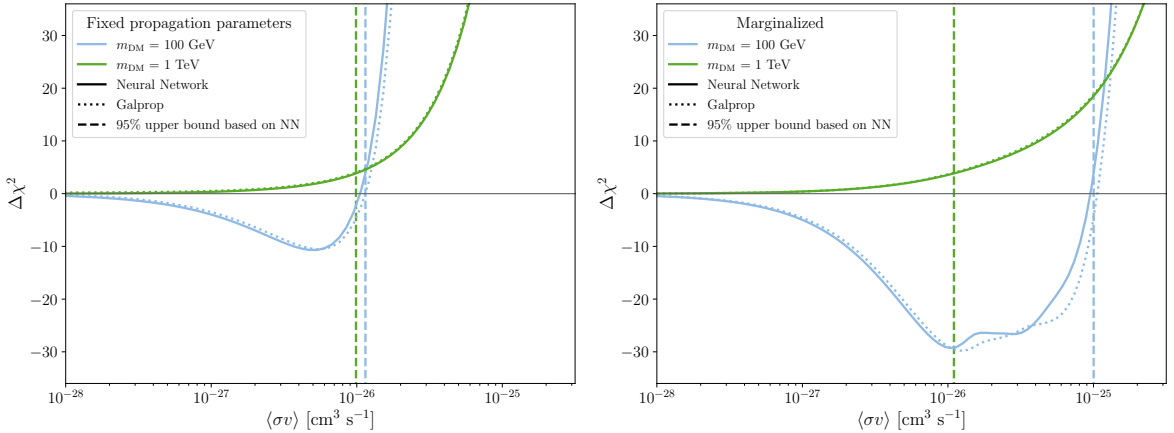


Figure 8. $\Delta\chi^2$ for the AMS-02 antiproton measurement based on the antiproton fluxes provided by the Neural Network and GALPROP as a function of $\langle\sigma v\rangle$ and for different values of m_{DM} . We assume a dominant DM $\text{DM} \rightarrow b\bar{b}$ annihilation in each case. *Left:* Propagation parameters are fixed to the best-fit values in a frequentist setup when only secondary antiprotons are considered (see table 1). *Right:* Propagation parameters are marginalized over using importance sampling. We also include the 95 % upper bound values of the annihilation cross section following eq. (4.9).

propagation parameters (left) and when marginalising over propagation parameters (right). The colour shading indicates parameter regions where $\Delta\chi^2 > 0$, such that a DM signal is disfavoured, while greyscale is used to indicate parameter regions where $\Delta\chi^2 < 0$ such that a DM signal is preferred. We find that this is the case for DM masses in the range 50–250 GeV. Again, marginalisation leads to relaxed exclusion bounds and an increased preference for a DM signal. We reiterate however that the magnitude of this preference is likely overestimated in our analysis.

To assess the impact of marginalisation let us finally compare our results with those obtained using a profile likelihood. As discussed in section 4.1, special care needs to be taken when using the ANN predictions to calculate a profile likelihood in order to ensure that the result is not dominated by regions of parameter space with insufficient training data. We achieve this goal by restricting the allowed parameter regions as follows: $0.1 < s < 0.6$, $1 \text{ GV} < R_0 < 10 \text{ GV}$, $0.35 < \delta < 0.6$ and $2.3 < \gamma_{2,(p)} < 2.5$. We then use MULTINEST to explore the remaining parameter space for fixed values of the DM mass and varying annihilation cross section in order to find the largest value of $\langle\sigma v\rangle$ such that $\Delta\hat{\chi}^2(m_{\text{DM}}, \langle\sigma v\rangle) \equiv -2\Delta \log \hat{\mathcal{L}}((m_{\text{DM}}, \langle\sigma v\rangle)) < 3.84$. Repeating this procedure for different values of m_{DM} then yields the exclusion limit.

The results are shown in figure 10 together with the exclusion limits obtained for fixed propagation parameters and when marginalising over propagation parameters as shown in figure 9. We find that in most regions of parameter space the profile likelihood approach yields somewhat weaker exclusion limits than the marginalisation. Such a difference is to be expected whenever substantial tuning in the propagation parameters is required in order to accommodate a DM signal. For example, for $m_{\text{DM}} = 1 \text{ TeV}$ and $\langle\sigma v\rangle = 5 \times 10^{-26} \text{ cm}^3 \text{ s}^{-1}$ we find that $\Delta\hat{\chi}^2 < 3.84$ can be achieved only if D_0 , $v_{0,c}$ and z_h all take values close to their lower bounds. Such a tuning is not penalised in the profile likelihood, but the contribution of these solutions to the marginalised likelihood will be suppressed according to the small volume of the viable parameter space. The same conclusion can be reached from the right

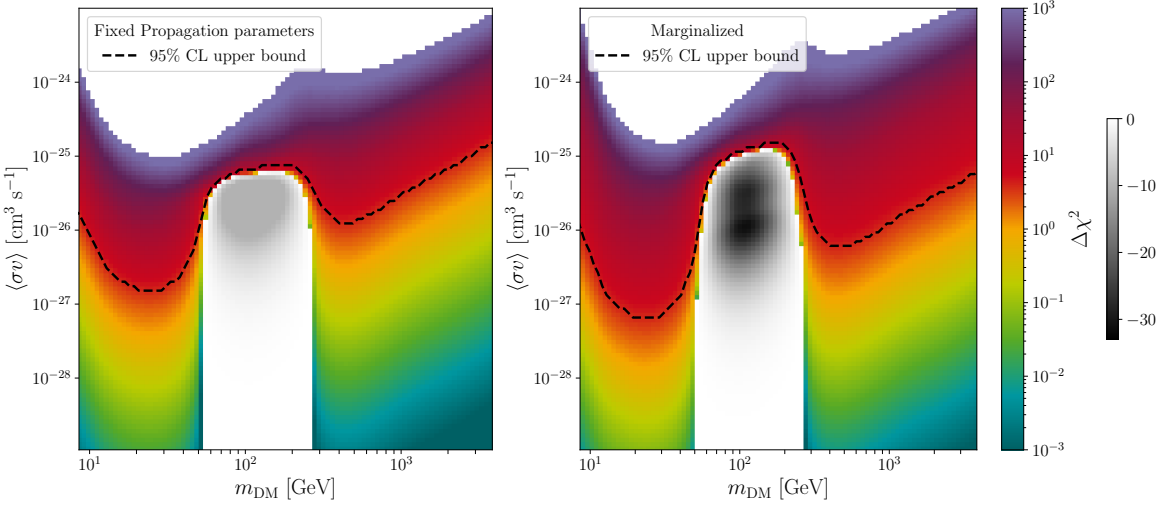


Figure 9. $\Delta\chi^2$ for the AMS-02 antiproton measurement as a function of $\langle\sigma v\rangle$ and m_{DM} using fixed propagation parameters (*left*) and performing the marginalisation via importance sampling (*right*). The dashed lines represent the 95 % CL upper bounds on the annihilation cross section. The white regions in the upper part of each panel correspond to $\Delta\chi^2 > 1000$ and are excluded to improve numerical stability.

panel of figure 7: Although there are sets of propagation parameters that yield $\Delta\chi^2 \approx 0$, most parameter combinations give significantly larger $\Delta\chi^2$, such that marginalisation leads to $\Delta\hat{\chi}^2 \approx 2.6$, close to the 95% confidence level upper bound. In other words, the difference between the two approaches is a direct consequence of the different statistical methods and not an artefact of the ANN predictions.

These differences are particularly relevant given how they affect the conclusions drawn from figure 10. When using the marginalised likelihood we find that the thermal cross section (indicated by the black dashed line) can be excluded for DM masses in the range 300–2000 GeV, implying that WIMP models in this mass range can only be viable if the injection of antiprotons are suppressed. When using the profile likelihood, on the other hand, almost the entire mass range above 70 GeV is found to be viable.

4.3 Example B: Scalar Singlet Dark Matter

We now illustrate the use of the ANN for the analysis of a specific model of DM with a singlet scalar field S . Imposing a Z_2 symmetry, $S \rightarrow -S$, the scalar particle is stable and thus a DM candidate. The Lagrangian of this scalar singlet DM (SSDM) model reads [95–97]

$$\mathcal{L} = \mathcal{L}_{\text{SM}} + \frac{1}{2}\partial_\mu S\partial^\mu S - \frac{1}{2}m_{S,0}^2 S^2 - \frac{1}{4}\lambda_S S^4 - \frac{1}{2}\lambda_{HS} S^2 H^\dagger H, \quad (4.10)$$

where \mathcal{L}_{SM} is the Standard Model Lagrangian and H is the Standard Model Higgs field. After electroweak symmetry breaking, the last three terms of the Lagrangian become

$$\mathcal{L} \supset -\frac{1}{2}m_S^2 S^2 - \frac{1}{4}\lambda_S S^4 - \frac{1}{4}\lambda_{HS} h^2 S^2 - \frac{1}{2}\lambda_{HS} vhS^2, \quad (4.11)$$

with $H = (h + v, 0)/\sqrt{2}$, $v = 246$ GeV, and where we introduced the physical mass of the singlet field, $m_S^2 = m_{S,0}^2 + \lambda_{HS} v^2/2$. The DM phenomenology of the SSDM has been extensively studied in the literature, see e.g. [37, 98–100] and references therein.

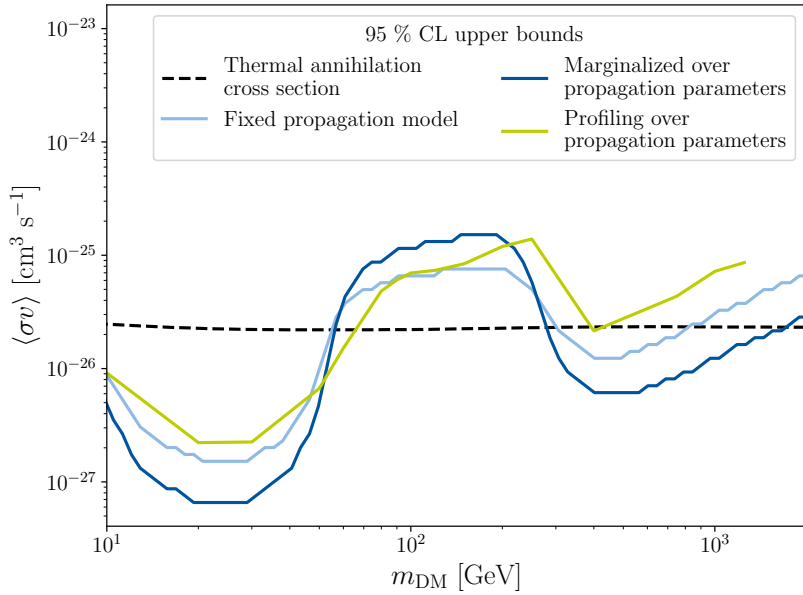


Figure 10. A comparison of the 95 % CL exclusion bounds in figure 9 (blue and light blue) with the bounds obtained when profiling over the propagation parameters using the CR spectra provided by our ANNs (green). The black dashed line indicates the thermal annihilation cross section for WIMPs from [94].

The DM phenomenology of the SSDM is fully specified by the mass of the DM particle, $m_S = m_{\text{DM}}$, and the strength of the coupling between the DM and Higgs particle, λ_{HS} . Below the Higgs-pair threshold, $m_S < m_h$, DM annihilation proceeds through s -channel Higgs exchange only, and the relative weight of the different SM final states is determined by the SM Higgs branching ratios, independent of the Higgs-scalar coupling λ_{HS} . Above the Higgs-pair threshold, $m_S \geq m_h$, the hh final state opens up. The strength of the annihilation into Higgs pairs, as compared to W , Z or top-quark pairs, depends on the size of the Higgs-scalar coupling. For our specific analysis we require that the SSDM provide the correct DM relic density, $\Omega h^2 = 0.1198 \pm 0.0015$ [101], which in turn determines the size of λ_{HS} for any given DM mass m_S . The corresponding branching fractions for DM annihilation within the SSDM are shown in Figure 11 (left panel) as a function of the DM mass.

Using the ANN we analyse the $\Delta\chi^2$ distribution of the model, marginalizing over propagation uncertainties as described in Section 4.1. The result is shown in Figure 11 (right panel). Comparing Figure 11 with the analogous result for the single annihilation channel into $b\bar{b}$, Figure 9 (right panel), we observe a similar overall shape of the $\Delta\chi^2$ distribution.

For light DM the SSDM annihilates dominantly into bottom final states, so one expects results that are very similar to the case of the single $b\bar{b}$ channel. However, for the smallest DM masses that we consider ($m_\chi \approx 10 \text{ GeV}$) we find that the constraints become considerably stronger when including even a sub-dominant contribution from $c\bar{c}$. The reason is that in this mass range, most antiprotons resulting from annihilation into bottom quarks have energies below 5 GeV and do therefore not give a contribution in our fits. Annihilation into charm quarks, on the other hand, can give rise to more energetic antiprotons, leading to stronger constraints. For DM masses above about 50 GeV, a variety of SM final states contributes in the SSDM, including in particular WW , hh and ZZ . However, as shown in [43], the limits for

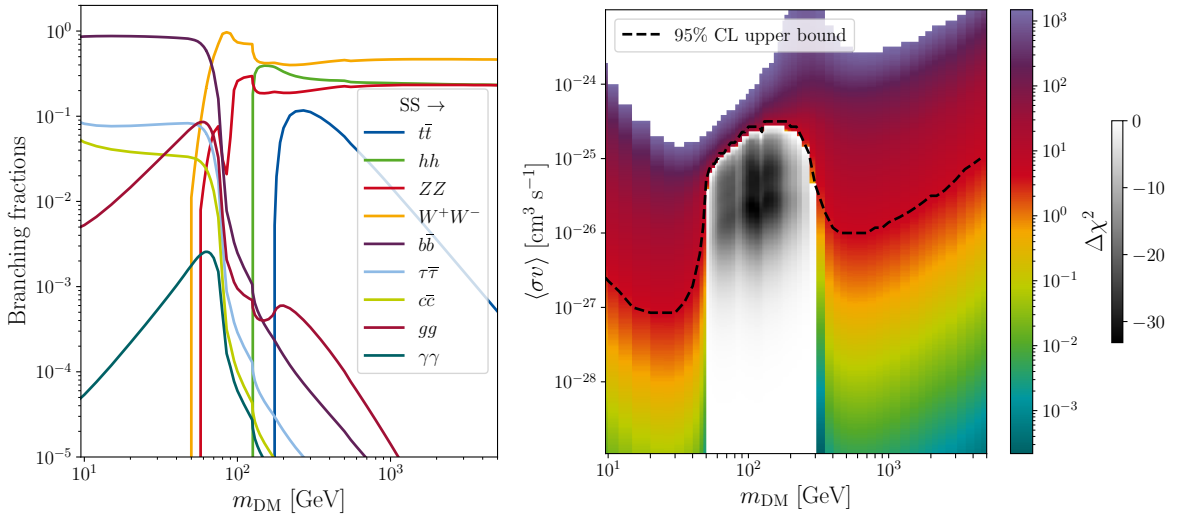


Figure 11. *Left:* Mass dependence of branching fractions of $SS \rightarrow \text{SM SM}$ in the SSDM model. *Right:* Marginal χ^2 distribution of the $\langle \sigma v \rangle - m_{\text{DM}}$ parameter space in the SSDM model.

heavy DM are similar for these final states and for annihilation into bottom quarks, so that the overall constraints for the SSDM are comparable to those for annihilation into bottom quarks only.

5 Conclusions

The analysis of cosmic ray (CR) antiprotons is a powerful method for the indirect detection of dark matter (DM). The accurate experimental measurements, in particular from AMS-02, allow to probe DM annihilation cross sections close to the value predicted by thermal freeze-out for a wide range of DM masses. However, a precise description of CR propagation through the Galaxy is required to exploit the potential of the experimental data. The propagation models depend on a large number of parameters, and the standard numerical simulation tools, such as GALPROP, are computationally expensive. Therefore, global analyses of generic models of DM can only be carried out with an immense computational effort, if at all.

In this work we have developed an artificial neural network (ANN) that allows extremely fast and accurate predictions of the cosmic ray flux for generic DM models. Specifically, we have employed recurrent neural networks (RNNs) to predict the CR energy spectrum. RNNs are particularly well suited to learn the correlations between the fluxes contained in neighbouring energy bins. Additional improvements in performance are achieved by grouping input parameters that are expected to have similar effects and by performing a suitable rescaling of the output spectra.

We have trained the ANN with a large set of antiproton fluxes simulated with GALPROP, where the propagation parameters have been chosen to be broadly compatible with the most recent AMS-02 data, and a generic parametrisation of the dark matter model in terms of the DM mass and the branching fractions for the annihilation into various Standard Model final states. We emphasise that the contribution of different DM models to the antiproton flux only has a marginal impact on the preferred range of the propagation parameters. It is therefore possible to focus the training of the ANN on the relevant range of propagation parameters without specifying the details of the DM model in advance. We have validated

the performance and accuracy of the network by comparing both the predicted antiproton fluxes and the resulting AMS-02 likelihoods to the ones obtained from explicit GALPROP simulations for a range of different propagation and DM model parameters.

We have then used the neural network predictions to test specific DM models against current AMS-02 data. We have focused on the DM parameter space and treated the propagation parameters as nuisance parameters by calculating both the corresponding profile and marginalised likelihoods. While the former approach requires an explicit restriction of the parameter space to the regions where the ANN has been sufficiently trained, this requirement can be automatically fulfilled in the latter case by employing importance sampling.

For DM annihilation into bottom quarks we have obtained results that are consistent with previous studies based on simulations and a profile likelihood approach. We find more stringent bounds on the DM parameter space when using the marginalised likelihood; here a thermal cross section can be excluded for DM annihilating fully into bottom quarks for DM masses in the range between approximately 300 GeV and 2 TeV. To illustrate the flexibility of our approach, we have also used the ANN to derive constraints on scalar singlet DM, for which DM annihilation results in a variety of Standard Model final states with branching fractions that depend strongly on the DM mass.

The ANN developed in this work, and the corresponding method for efficient training, can be easily extended to alternative propagation models and can be applied to a wide class of DM scenarios. It will thus be possible to fully exploit the potential of current and future cosmic-ray data in global analyses of general DM models. The fully trained networks together with a suitable user interface are publicly available at <https://github.com/kathrinnp/DarkRayNet>.

Acknowledgments

We thank ... for discussions. This work is funded by the Deutsche Forschungsgemeinschaft (DFG) through the Collaborative Research Center TRR 257 “Particle Physics Phenomenology after the Higgs Discovery” under Grant 396021762 - TRR 257 and the Emmy Noether Grant No. KA 4662/1-1. Simulations and ANN training were performed with computing resources granted by RWTH Aachen University under project jara0184.

A Predicting Proton and Helium Spectra

When simulating the antiproton fluxes as described in section 3.1 we automatically also obtain the CR spectra of protons, deuterium, and helium (${}^3\text{He}$ and ${}^4\text{He}$). The task of modelling these spectra using an ANN is very comparable with the task fulfilled by the sNet. We have thus examined the ability of the sNet architecture (as described in sec. 3.2) to also accurately predict proton and helium spectra. The inputs of the sNet remain the same, but we have extended the length of the final output layer, to accommodate a wider energy range, appropriate for the proton and Helium AMS-02 and Voyager data. Using also the same training process (see sec. 3.3) we achieve a similar accuracy as for the secondary antiprotons, as each of the predictions deviates from the simulations only marginally with respect to the experimental uncertainties. In figures 12 and 13 we show exemplary results for protons, resp. helium, and their individual components analogous to figure 5.

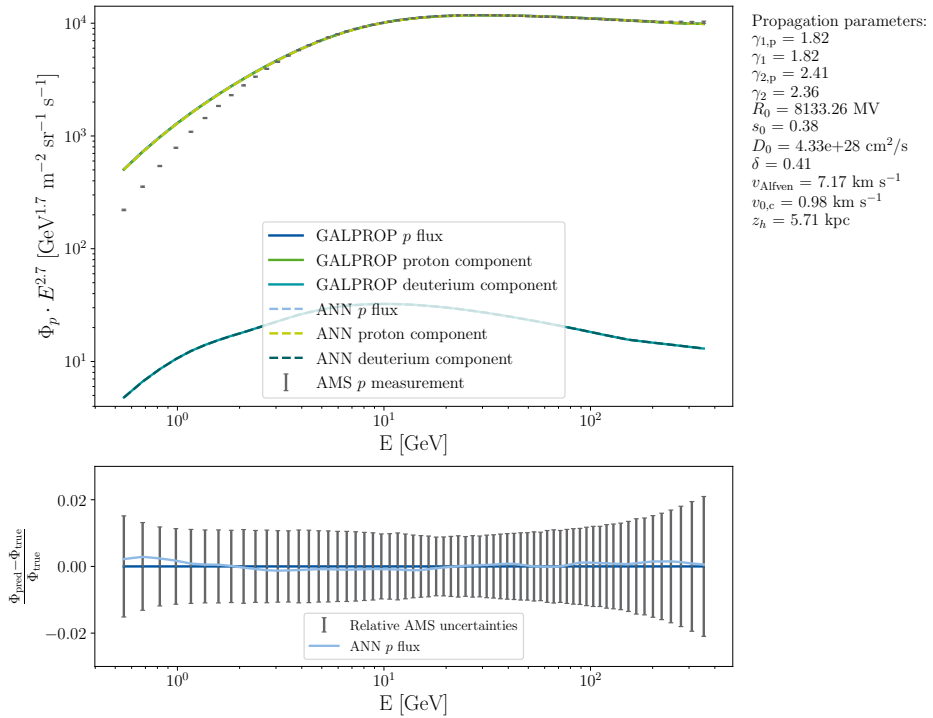


Figure 12. Exemplary comparison of the simulated vs predicted protons flux of the individual components protons and Deuterium and the combination of both where the listed parameters and simulated fluxes are randomly sampled from the test set. Each component of the neural network flux is predicted by the individual networks. The lower panel depicts the relative difference between the simulated and predicted fluxes with respect to the simulated flux compared to the relative AMS-02 uncertainty.

References

- [1] **Fermi-LAT Collaboration**, M. Ackermann et al., *Dark Matter Constraints from Observations of 25 Milky Way Satellite Galaxies with the Fermi Large Area Telescope*, *Phys. Rev.* **D89** (2014) 042001, [[1310.0828](#)].
- [2] **Fermi-LAT Collaboration**, M. Ackermann et al., *Searching for Dark Matter Annihilation from Milky Way Dwarf Spheroidal Galaxies with Six Years of Fermi Large Area Telescope Data*, *Phys. Rev. Lett.* **115** (2015), no. 23 231301, [[1503.02641](#)].
- [3] **Fermi-LAT Collaboration**, M. Ackermann et al., *Updated search for spectral lines from Galactic dark matter interactions with pass 8 data from the Fermi Large Area Telescope*, *Phys. Rev.* **D91** (2015), no. 12 122002, [[1506.00013](#)].
- [4] **AMS Collaboration**, M. Aguilar et al., *The Alpha Magnetic Spectrometer (AMS) on the international space station: Part II — Results from the first seven years*, *Phys. Rept.* **894** (2021) 1–116.
- [5] A. W. Strong, I. V. Moskalenko, and O. Reimer, *Diffuse continuum gamma-rays from the galaxy*, *Astrophys. J.* **537** (2000) 763–784, [[astro-ph/9811296](#)]. [Erratum: *Astrophys. J.* **541**, 1109(2000)].
- [6] C. Evoli, D. Gaggero, D. Grasso, and L. Maccione, *Cosmic-Ray Nuclei, Antiprotons and Gamma-rays in the Galaxy: a New Diffusion Model*, *JCAP* **0810** (2008) 018, [[0807.4730](#)]. [Erratum: *JCAP* **1604**, no. 04, E01(2016)].

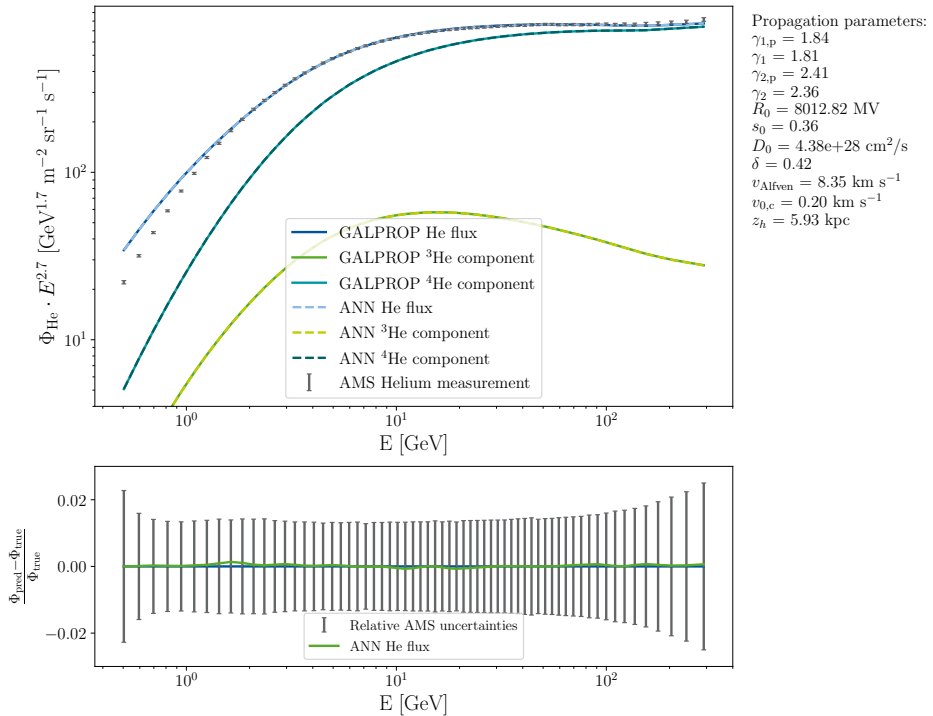


Figure 13. Exemplary comparison of the simulated vs predicted protons flux of the individual components ${}^3\text{He}$ and ${}^4\text{He}$ and the combination of both where the listed parameters and simulated fluxes are randomly sampled from the test set. Each component of the neural network flux is predicted by the individual networks. The lower panel depicts the relative difference between the simulated and predicted fluxes with respect to the simulated flux compared to the relative AMS-02 uncertainty.

- [7] A. Cuoco, M. Krämer, and M. Korsmeier, *Novel Dark Matter Constraints from Antiprotons in Light of AMS-02*, *Phys. Rev. Lett.* **118** (2017), no. 19 191102, [[1610.03071](#)].
- [8] M.-Y. Cui, Q. Yuan, Y.-L. S. Tsai, and Y.-Z. Fan, *Possible dark matter annihilation signal in the AMS-02 antiproton data*, *Phys. Rev. Lett.* **118** (2017), no. 19 191101, [[1610.03840](#)].
- [9] A. Reinert and M. W. Winkler, *A Precision Search for WIMPs with Charged Cosmic Rays*, *JCAP* **1801** (2018), no. 01 055, [[1712.00002](#)].
- [10] I. Cholis, T. Linden, and D. Hooper, *A Robust Excess in the Cosmic-Ray Antiproton Spectrum: Implications for Annihilating Dark Matter*, *Phys. Rev.* **D99** (2019), no. 10 103026, [[1903.02549](#)].
- [11] P. Blasi and P. D. Serpico, *High-energy antiprotons from old supernova remnants*, *Phys. Rev. Lett.* **103** (2009) 081103, [[0904.0871](#)].
- [12] P. Mertsch and S. Sarkar, *AMS-02 data confront acceleration of cosmic ray secondaries in nearby sources*, *Phys. Rev.* **D90** (2014) 061301, [[1402.0855](#)].
- [13] P. Mertsch, A. Vittino, and S. Sarkar, *Explaining cosmic ray antimatter with secondaries from old supernova remnants*, [2012.12853](#).
- [14] T. Aramaki et al., *Review of the theoretical and experimental status of dark matter identification with cosmic-ray antideuterons*, *Phys. Rept.* **618** (2016) 1–37, [[1505.07785](#)].
- [15] P. von Doetinchem et al., *Cosmic-ray antinuclei as messengers of new physics: status and outlook for the new decade*, *JCAP* **08** (2020) 035, [[2002.04163](#)].

- [16] L. Bergstrom, J. Edsjo, and P. Ullio, *Cosmic anti-protons as a probe for supersymmetric dark matter?*, *Astrophys. J.* **526** (1999) 215–235, [[astro-ph/9902012](#)].
- [17] F. Donato, N. Fornengo, D. Maurin, and P. Salati, *Antiprotons in cosmic rays from neutralino annihilation*, *Phys. Rev.* **D69** (2004) 063501, [[astro-ph/0306207](#)].
- [18] T. Bringmann and P. Salati, *The galactic antiproton spectrum at high energies: Background expectation vs. exotic contributions*, *Phys. Rev.* **D75** (2007) 083006, [[astro-ph/0612514](#)].
- [19] F. Donato, D. Maurin, P. Brun, T. Delahaye, and P. Salati, *Constraints on WIMP Dark Matter from the High Energy PAMELA \bar{p}/p data*, *Phys. Rev. Lett.* **102** (2009) 071301, [[0810.5292](#)].
- [20] N. Fornengo, L. Maccione, and A. Vittino, *Constraints on particle dark matter from cosmic-ray antiprotons*, *JCAP* **1404** (2014), no. 04 003, [[1312.3579](#)].
- [21] C. Evoli, I. Cholis, D. Grasso, L. Maccione, and P. Ullio, *Antiprotons from dark matter annihilation in the Galaxy: astrophysical uncertainties*, *Phys. Rev.* **D85** (2012) 123511, [[1108.0664](#)].
- [22] T. Bringmann, M. Vollmann, and C. Weniger, *Updated cosmic-ray and radio constraints on light dark matter: Implications for the GeV gamma-ray excess at the Galactic center*, *Phys. Rev.* **D90** (2014), no. 12 123001, [[1406.6027](#)].
- [23] V. Pettorino, G. Busoni, A. De Simone, E. Morgante, A. Riotto, et al., *Can AMS-02 discriminate the origin of an anti-proton signal?*, *JCAP* **1410** (2014), no. 10 078, [[1406.5377](#)].
- [24] M. Cirelli, D. Gaggero, G. Giesen, M. Taoso, and A. Urbano, *Antiproton constraints on the GeV gamma-ray excess: a comprehensive analysis*, *JCAP* **1412** (2014), no. 12 045, [[1407.2173](#)].
- [25] J. A. R. Cembranos, V. Gammaldi, and A. L. Maroto, *Antiproton signatures from astrophysical and dark matter sources at the galactic center*, *JCAP* **1503** (2015), no. 03 041, [[1410.6689](#)].
- [26] D. Hooper, T. Linden, and P. Mertsch, *What Does The PAMELA Antiproton Spectrum Tell Us About Dark Matter?*, *JCAP* **1503** (2015), no. 03 021, [[1410.1527](#)].
- [27] M. Boudaud, M. Cirelli, G. Giesen, and P. Salati, *A fussy revisit of antiprotons as a tool for Dark Matter searches*, *JCAP* **1505** (2015), no. 05 013, [[1412.5696](#)].
- [28] G. Giesen, M. Boudaud, Y. Genolini, V. Poulin, M. Cirelli, et al., *AMS-02 antiprotons, at last! Secondary astrophysical component and immediate implications for Dark Matter*, *JCAP* **1509** (2015), no. 09 023, [[1504.04276](#)].
- [29] C. Evoli, D. Gaggero, and D. Grasso, *Secondary antiprotons as a Galactic Dark Matter probe*, *JCAP* **1512** (2015), no. 12 039, [[1504.05175](#)].
- [30] P. D. L. T. Luque, *Combined analyses of the antiproton production from cosmic-ray interactions and its possible dark matter origin*, [2107.06863](#).
- [31] M. Di Mauro and M. W. Winkler, *Multimessenger constraints on the dark matter interpretation of the Fermi-LAT Galactic center excess*, *Phys. Rev. D* **103** (2021), no. 12 123005, [[2101.11027](#)].
- [32] A. Cuoco, J. Heisig, L. Klamt, M. Korsmeier, and M. Krämer, *Scrutinizing the evidence for dark matter in cosmic-ray antiprotons*, *Phys. Rev.* **D99** (2019), no. 10 103014, [[1903.01472](#)].
- [33] M. Boudaud, Y. Génolini, L. Derome, J. Lavalle, D. Maurin, et al., *AMS-02 antiprotons' consistency with a secondary astrophysical origin*, *Phys. Rev. Res.* **2** (2020), no. 2 023022, [[1906.07119](#)].
- [34] J. Heisig, M. Korsmeier, and M. W. Winkler, *Dark matter or correlated errors: Systematics of*

the AMS-02 antiproton excess, *Phys. Rev. Res.* **2** (2020), no. 4 043017, [[2005.04237](#)].

- [35] J. Heisig, *Cosmic-ray antiprotons in the AMS-02 era: A sensitive probe of dark matter,* *Mod. Phys. Lett. A* **36** (2021), no. 05 2130003, [[2012.03956](#)].
- [36] M. Cirelli, G. Corcella, A. Hektor, G. Hutsi, M. Kadastik, et al., *PPPC 4 DM ID: A Poor Particle Physicist Cookbook for Dark Matter Indirect Detection,* *JCAP* **1103** (2011) 051, [[1012.4515](#)]. [Erratum: *JCAP*1210,E01(2012)].
- [37] A. Cuoco, J. Heisig, M. Korsmeier, and M. Krämer, *Probing dark matter annihilation in the Galaxy with antiprotons and gamma rays,* *JCAP* **1710** (2017), no. 10 053, [[1704.08258](#)].
- [38] J. F. Navarro, C. S. Frenk, and S. D. M. White, *The Structure of cold dark matter halos,* *Astrophys. J.* **462** (1996) 563–575, [[astro-ph/9508025](#)].
- [39] P. Salucci, F. Nesti, G. Gentile, and C. F. Martins, *The dark matter density at the Sun’s location,* *Astron. Astrophys.* **523** (2010) A83, [[1003.3101](#)].
- [40] P. F. de Salas and A. Widmark, *Dark matter local density determination: recent observations and future prospects,* [2012.11477](#).
- [41] M. Benito, A. Cuoco, and F. Iocco, *Handling the Uncertainties in the Galactic Dark Matter Distribution for Particle Dark Matter Searches,* *JCAP* **03** (2019) 033, [[1901.02460](#)].
- [42] A. Burkert, *The Structure of dark matter halos in dwarf galaxies,* *IAU Symp.* **171** (1996) 175, [[astro-ph/9504041](#)]. [*Astrophys. J.*447,L25(1995)].
- [43] A. Cuoco, J. Heisig, M. Korsmeier, and M. Krämer, *Constraining heavy dark matter with cosmic-ray antiprotons,* *JCAP* **1804** (2018), no. 04 004, [[1711.05274](#)].
- [44] M. di Mauro, F. Donato, A. Goudelis, and P. D. Serpico, *New evaluation of the antiproton production cross section for cosmic ray studies,* *Phys. Rev.* **D90** (2014), no. 8 085017, [[1408.0288](#)]. [Erratum: *Phys. Rev.*D98,no.4,049901(2018)].
- [45] M. W. Winkler, *Cosmic Ray Antiprotons at High Energies,* *JCAP* **1702** (2017), no. 02 048, [[1701.04866](#)].
- [46] M. Korsmeier, F. Donato, and M. Di Mauro, *Production cross sections of cosmic antiprotons in the light of new data from the NA61 and LHCb experiments,* *Phys. Rev.* **D97** (2018), no. 10 103019, [[1802.03030](#)].
- [47] M. Kachelrieß, I. V. Moskalenko, and S. Ostapchenko, *AAfrag: Interpolation routines for Monte Carlo results on secondary production in proton-proton, proton-nucleus and nucleus-nucleus interactions,* [1904.05129](#).
- [48] F. Donato, M. Korsmeier, and M. Di Mauro, *Prescriptions on antiproton cross section data for precise theoretical antiproton flux predictions,* *Phys. Rev.* **D96** (2017), no. 4 043007, [[1704.03663](#)].
- [49] I. V. Moskalenko, A. W. Strong, J. F. Ormes, and M. S. Potgieter, *Secondary anti-protons and propagation of cosmic rays in the galaxy and heliosphere,* *Astrophys. J.* **565** (2002) 280–296, [[astro-ph/0106567](#)].
- [50] E. Amato and P. Blasi, *Cosmic ray transport in the Galaxy: A review,* *Adv. Space Res.* **62** (2018) 2731–2749, [[1704.05696](#)].
- [51] S. Gabici, C. Evoli, D. Gaggero, P. Lipari, P. Mertsch, et al., *The origin of Galactic cosmic rays: challenges to the standard paradigm,* *Int. J. Mod. Phys. D* **28** (2019), no. 15 1930022, [[1903.11584](#)].
- [52] O. Adriani et al., *Measurement of boron and carbon fluxes in cosmic rays with the PAMELA experiment,* *Astrophys. J.* **791** (2014), no. 2 93, [[1407.1657](#)].
- [53] E. C. Stone, A. C. Cummings, F. B. McDonald, B. C. Heikkila, N. Lal, et al., *Voyager 1*

Observes Low-Energy Galactic Cosmic Rays in a Region Depleted of Heliospheric Ions, *Science* **341** (Jul, 2013) 150–153.

- [54] Y. Génolini et al., *Cosmic-ray transport from AMS-02 boron to carbon ratio data: Benchmark models and interpretation*, *Phys. Rev. D* **99** (2019), no. 12 123028, [[1904.08917](#)].
- [55] C. Evoli, R. Aloisio, and P. Blasi, *Galactic cosmic rays after the AMS-02 observations*, *Phys. Rev. D* **99** (2019), no. 10 103023, [[1904.10220](#)].
- [56] C. Evoli, G. Morlino, P. Blasi, and R. Aloisio, *AMS-02 beryllium data and its implication for cosmic ray transport*, *Phys. Rev. D* **101** (2020), no. 2 023013, [[1910.04113](#)].
- [57] M. Boschini et al., *Deciphering the local Interstellar spectra of primary cosmic ray species with HelMod*, *Astrophys. J.* **858** (2018), no. 1 61, [[1804.06956](#)].
- [58] M. Boschini et al., *Deciphering the local Interstellar spectra of secondary nuclei with GALPROP/HelMod framework and a hint for primary lithium in cosmic rays*, [1911.03108](#).
- [59] N. Weinrich, Y. Genolini, M. Boudaud, L. Derome, and D. Maurin, *Combined analysis of AMS-02 (Li,Be,B)/C, N/O, 3He, and 4He data*, *Astron. Astrophys.* **639** (2020) A131, [[2002.11406](#)].
- [60] N. Weinrich, M. Boudaud, L. Derome, Y. Genolini, J. Lavalle, et al., *Galactic halo size in the light of recent AMS-02 data*, *Astron. Astrophys.* **639** (2020) A74, [[2004.00441](#)].
- [61] P. D. L. T. Luque, M. N. Mazziotta, F. Loparco, F. Gargano, and D. Serini, *Markov chain Monte Carlo analyses of the flux ratios of B, Be and Li with the DRAGON2 code*, [2102.13238](#).
- [62] P. De La Torre Luque, M. N. Mazziotta, F. Loparco, F. Gargano, and D. Serini, *Implications of current nuclear cross sections on secondary cosmic rays with the upcoming DRAGON2 code*, *JCAP* **03** (2021) 099, [[2101.01547](#)].
- [63] B. Schroer, C. Evoli, and P. Blasi, *Heavy Galactic cosmic-ray nuclei: the case of new AMS-02 measurements*, [2102.12576](#).
- [64] M. Korsmeier and A. Cuoco, *Implications of Lithium to Oxygen AMS-02 spectra on our understanding of cosmic-ray diffusion*, *Phys. Rev. D* **103** (2021), no. 10 103016, [[2103.09824](#)].
- [65] A. W. Strong, I. V. Moskalenko, and V. S. Ptuskin, *Cosmic-ray propagation and interactions in the Galaxy*, *Ann. Rev. Nucl. Part. Sci.* **57** (2007) 285–327, [[astro-ph/0701517](#)].
- [66] A. W. Strong, *Recent extensions to GALPROP*, [1507.05020](#).
- [67] A. Putze, L. Derome, and D. Maurin, *A Markov Chain Monte Carlo technique to sample transport and source parameters of Galactic cosmic rays: II. Results for the diffusion model combining B/C and radioactive nuclei*, *Astron. Astrophys.* **516** (2010) A66, [[1001.0551](#)].
- [68] D. Maurin, *USINE: semi-analytical models for Galactic cosmic-ray propagation*, [1807.02968](#).
- [69] C. Evoli, D. Gaggero, A. Vittino, M. Di Mauro, D. Grasso, et al., *Cosmic-ray propagation with DRAGON2: II. Nuclear interactions with the interstellar gas*, *JCAP* **1807** (2018), no. 07 006, [[1711.09616](#)].
- [70] R. Kissmann, *PICARD: A novel code for the Galactic Cosmic Ray propagation problem*, *Astropart. Phys.* **55** (2014) 37–50, [[1401.4035](#)].
- [71] D. A. Green, *Constraints on the distribution of supernova remnants with Galactocentric radius*, *Mon. Not. Roy. Astron. Soc.* **454** (2015), no. 2 1517–1524, [[1508.02931](#)].
- [72] M. Korsmeier and A. Cuoco, *Galactic cosmic-ray propagation in the light of AMS-02: Analysis of protons, helium, and antiprotons*, *Phys. Rev. D* **94** (2016), no. 12 123019, [[1607.06093](#)].
- [73] V. A. Dogiel, V. S. Berezinsky, S. V. Bulanov, and V. S. Ptuskin, *Astrophysics of cosmic rays*. Elsevier Since Publischers B.V., 1990.

- [74] E. S. Seo and V. S. Ptuskin, *Stochastic reacceleration of cosmic rays in the interstellar medium*, *Astrophys. J.* **431** (Aug., 1994) 705–714.
- [75] L. A. Fisk, *Solar Modulation and a Galactic Origin for the Anomalous Component Observed in Low-Energy Cosmic Rays*, *Astrophys. J.* **206** (1976) 333–341.
- [76] R. Kappl, *SOLARPROP: Charge-sign Dependent Solar Modulation for Everyone*, *Comput. Phys. Commun.* **207** (2016) 386–399, [[1511.07875](#)].
- [77] A. Vittino, C. Evoli, and D. Gaggero, *Cosmic-ray transport in the heliosphere with HelioProp*, *PoS ICRC2017* (2018) 024, [[1707.09003](#)].
- [78] M. J. Boschini, S. Della Torre, M. Gervasi, G. La Vacca, and P. G. Rancoita, *Propagation of cosmic rays in heliosphere: The HELMOD model*, *Adv. Space Res.* **62** (2018) 2859–2879, [[1704.03733](#)].
- [79] E. Fiandrini, N. Tomassetti, B. Bertucci, F. Donnini, M. Graziani, et al., *Numerical modeling of cosmic rays in the heliosphere: Analysis of proton data from AMS-02 and PAMELA*, *Phys. Rev. D* **104** (2021), no. 2 023012, [[2010.08649](#)].
- [80] M. D. Ngobeni, O. P. M. Aslam, D. Bisschoff, M. S. Potgieter, D. C. Ndiiwani, et al., *The 3D numerical modeling of the solar modulation of galactic protons and helium nuclei related to observations by PAMELA between 2006 and 2009*, *Astrophys. Space Sci.* **365** (2020), no. 11 182.
- [81] A. C. Cummings, E. C. Stone, B. C. Heikkila, N. Lal, W. R. Webber, et al., *Galactic Cosmic Rays in the Local Interstellar Medium: Voyager 1 Observations and Model Results*, *Astrophys. J.* **831** (2016), no. 1 18.
- [82] F. Feroz, M. P. Hobson, and M. Bridges, *MultiNest: an efficient and robust Bayesian inference tool for cosmology and particle physics*, *Mon. Not. Roy. Astron. Soc.* **398** (2009) 1601–1614, [[0809.3437](#)].
- [83] F. James and M. Roos, *Minuit: A System for Function Minimization and Analysis of the Parameter Errors and Correlations*, *Comput. Phys. Commun.* **10** (1975) 343–367.
- [84] **AMS Collaboration**, M. Aguilar et al., *Observation of New Properties of Secondary Cosmic Rays Lithium, Beryllium, and Boron by the Alpha Magnetic Spectrometer on the International Space Station*, *Phys. Rev. Lett.* **120** (2018), no. 2 021101.
- [85] **AMS Collaboration**, M. Aguilar et al., *Observation of the Identical Rigidity Dependence of He, C, and O Cosmic Rays at High Rigidities by the Alpha Magnetic Spectrometer on the International Space Station*, *Phys. Rev. Lett.* **119** (2017), no. 25 251101.
- [86] Y. Genolini et al., *Indications for a high-rigidity break in the cosmic-ray diffusion coefficient*, *Phys. Rev. Lett.* **119** (2017), no. 24 241101, [[1706.09812](#)].
- [87] A. Coccaro, M. Pierini, L. Silvestrini, and R. Torre, *The DNNLikelihood: enhancing likelihood distribution with Deep Learning*, *Eur. Phys. J. C* **80** (2020), no. 7 664, [[1911.03305](#)].
- [88] K. Cho, B. van Merriënboer, C. Gulcehre, D. Bahdanau, F. Bougares, et al., *Learning phrase representations using rnn encoder-decoder for statistical machine translation*, Oct., 2014.
- [89] S. Hochreiter and J. Schmidhuber, *Long short-term memory*, *Neural Computation* **9** (1997), no. 8 1735–1780.
- [90] F. Chollet et al., *Keras*, 2015.
- [91] M. Abadi, A. Agarwal, P. Barham, E. Brevdo, Z. Chen, et al., *TensorFlow: Large-scale machine learning on heterogeneous systems*, 2015. Software available from tensorflow.org.
- [92] D. P. Kingma and J. Ba, “Adam: A method for stochastic optimization.” Conference paper at the 3rd International Conference for Learning Representations, San Diego, 2015, 2017.

- [93] A. B. Owen, *Monte Carlo theory, methods and examples*. 2013.
- [94] G. Steigman, B. Dasgupta, and J. F. Beacom, *Precise relic wimp abundance and its impact on searches for dark matter annihilation*, *Phys. Rev. D* **86** (Jul, 2012) 023506.
- [95] V. Silveira and A. Zee, *SCALAR PHANTOMS*, *Phys. Lett.* **161B** (1985) 136–140.
- [96] J. McDonald, *Gauge singlet scalars as cold dark matter*, *Phys. Rev.* **D50** (1994) 3637–3649, [[hep-ph/0702143](#)].
- [97] C. P. Burgess, M. Pospelov, and T. ter Veldhuis, *The Minimal model of nonbaryonic dark matter: A Singlet scalar*, *Nucl. Phys.* **B619** (2001) 709–728, [[hep-ph/0011335](#)].
- [98] J. M. Cline, K. Kainulainen, P. Scott, and C. Weniger, *Update on scalar singlet dark matter*, *Phys. Rev.* **D88** (2013) 055025, [[1306.4710](#)]. [Erratum: Phys. Rev.D92,no.3,039906(2015)].
- [99] A. Beniwal, F. Rajec, C. Savage, P. Scott, C. Weniger, et al., *Combined analysis of effective Higgs portal dark matter models*, *Phys. Rev.* **D93** (2016), no. 11 115016, [[1512.06458](#)].
- [100] A. Cuoco, B. Eiteneuer, J. Heisig, and M. Krämer, *A global fit of the γ -ray galactic center excess within the scalar singlet Higgs portal model*, *JCAP* **1606** (2016), no. 06 050, [[1603.08228](#)].
- [101] **Planck Collaboration**, P. A. R. Ade et al., *Planck 2015 results. XIII. Cosmological parameters*, *Astron. Astrophys.* **594** (2016) A13, [[1502.01589](#)].